Master thesis : Study of a Cubesat dual band infrared imager for hydric stress observation from space

Auteur : Duenas Herrero, Antonio
Promoteur(s) : Loicq, Jerome
Faculté : Faculté des Sciences appliquées
Diplôme : Cours supplémentaires destinés aux étudiants d'échange (Erasmus, ...)
Année académique : 2018-2019
URI/URL : http://hdl.handle.net/2268.2/6598

UNIVERSITY OF LIÈGE

Faculty of Applied Sciences

Study of a CubeSat dual band infrared imager for hydric stress observation from space

---

Author:

Antonio Dueñas Herrero

Academic advisor:

Jerôme Loicq

Assistant:

Victor Laborde

Graduation Studies conducted for obtaining the Master's degree in Aerospace Engineering

Academic year 2018-2019

Abstract

CubeSats are one of the main projects for the present and future in space, specially in academic environments. Due to their low price, these nanosatellite are the perfect means for students to get involved in space missions and develop satellites from scratch. This is the case of OUTFI-Next (Orbital Utility For Thermal Imaging), the new CubeSat promoted by the University of Liege and the Centre Spatial de Liège.

After the success of OUFTI-1 (Orbital Utility For Telecommunication Innovation) which was launched in 2016 with the goal of providing support with D-STAR communication and the widely advanced OUFTI-2, which is expected to outperform OUFTI-1 characteristics, OUFTI-Next was conceived. The objective of this 3U CubeSat (30cm x 10cm x 10cm) is to provide a smart irrigation strategy of agricultural fields around the world. This will be carried out by measuring hydric stresses in crops, detecting lack of water in the plants by monitoring the leaf surface temperature with an infrared camera.

Now, in its third year of development, it has been thought about converting the demonstrator into a dual-band imager, working in Middle Wave Infra-Red (MWIR) and Long Wave Infra-Red (LWIR). The purpose of this document is to report the feasibility of this concept. To do so, the radiometric budget of the satellite in both bands, MWIR and LWIR, will be analyzed, as well as the Signal to Noise Ratio, considering the optics and the different types of detectors available.

Keywords: CubeSat, dual band, radiometry, Signal to Noise Ratio

Acknowledgements

En primer lugar, me gustaría dar las gracias a mi tutor, Jerôme Loicq, y a su asistente, Victor Laborde, por su inconmensurable apoyo y guía durante todo el proyecto, siempre dispuestos a resolver mis dudas. Me han ayudado a desarrollar mis capacidades ingenieriles en gran medida.

Seguidamente a mis compañeros del Erasmus, por llenarme un año de aventuras, a los de la carrera, por todo el sufrimiento compartido y a los míos, por esos grandes momentos.

Para terminar, este trabajo final de carrera se lo quiero dedicar a mi familia, mis abuelos, tíos y primos. Concretamente quiero mencionar a mi padre Antonio, mi madre Carolina, mi hermano Rodrigo y mis primos Antonio y Marta, que siempre han creído en mí y cuyo cariño me ha permitido seguir adelante.

A Elvira, gracias por el viaje.

Contents

List of Figures

List of Tables

Acronyms

ADCS Attitude Determination and Control System

ARC AntiReflective Coating

BB Black Body

CSL Centre Spatial de Liège

ECOSTRESS ECOsystem Spaceborne Thermal Radiometer Experiment on Space Station

EMR Electromagnetic radiation

FOV Field of View

GSD Ground Sampling Distance

iFOV Instantaneous Field of View

IGBP International Geosphere Biosphere Programme

IR Infra-Red

ISS International Space Station

JHU Johns Hopkins University

JPL Jet Propulsion Laboratory

LWIR Long Wave Infra-Red

MLI Multi-Layer Insulation

MWIR Middle Wave Infra-Red

NASA National Aeronautic and Space Administration

NETD Noise Equivalent Temperature Difference

OBC On-Board Computer

OUFTI-1 Orbital Utility For Telecommunication Innovation

OUFTI-Next Orbital Utility For Thermal Imaging

PCB Printed Circuit Board

RH Relative Humidity

SNR Signal to Noise Ratio

SSO Sun Synchronous Orbit

SWIR Short Wave Infra-Red

TTC Thermal Time Constant

UHF Ultra High Frequency

USGS-Reston United States Geological Survey

VHF Very High Frequency

VIS Visible Spectrum

1 Introduction

First of all, the scientific motivation of the project will be presented in order to explain how the technology employed works and the potential applications that the demonstrator could generate, giving a step forward towards the solution of problems related with limiting the amount of water wasted and improving the productivity of agricultural fields. After that, OUFTI-Next mission will be introduced, detailing the base idea and the main characteristics of the satellite. Finally, the requirements and constraints of the spacecraft and its orbit will be stated by informing about the work already carried out for other students in their master's thesis.

1.1 Scientific purpose

Without any doubt, food and agriculture industries are the two biggest consumers of water as they require two orders of magnitude more of it than what it is consumed for personal needs.

It is possible to roughly calculate global water requirements for food crops through the specific needs for one adult based on their caloric intake per day, which is approximately 2800 kcal [12]. This would mean 1000 m^3 of water per year to produce the necessary [13]. If one assumes that the world population is about 6 billion people, the amount of water would be 6000 km^3 to feed the globe.

The majority of water entailed with agriculture comes directly from rainfall and, although it varies depending on climate conditions and the development of irrigation infrastructure (see Figure 1.1), it can be assumed that, as a global average, only 15% comes from irrigation. However, up to almost 70% of drinkable water obtained from rivers, lakes and aquifers is withdrawn to irrigate agricultural fields [13]. Consequently, irrigation, based on this theory, would need 900 km^3 of water per year for food production. In addition, only about 40% of freshwater effectively contributes to crop production due to evaporation and losses in the irrigation system. Therefore, the current global water allocated for irrigation is estimated as 2500 km^3 per year, which supposes a huge amount of water.

In order to improve that digit, water-saving technologies have been created over the last century, such as underground drip irrigation. Nowadays, new and amazing technologies are developing, some of them related with space.

Through these technologies, daily monitoring of crops has passed from an ideal dream to a soon reality. To do so, water stress, also known as hydric or osmotic stress, is measured.

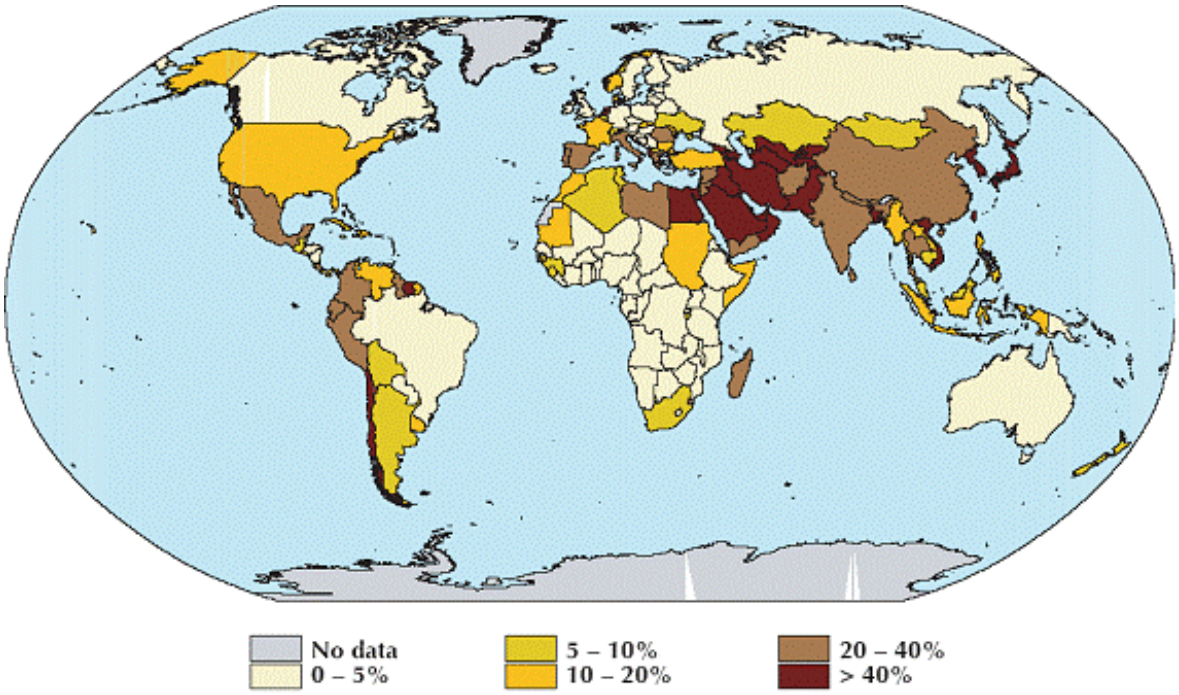

Figure 1.1: Irrigation percentage per country

Water stress is defined by biologists as the stress that a plant undergoes in environmental conditions where the quantity of water transpired by the plant is higher than the quantity that it absorbs [14]. In other words, well when the transpiration rate becomes intense, or well when the plant demands more water than available or the quality of water absorbed is not enough to palliate the necessities of the crop in a certain period of time.

This stress is normally provoked by drought, but it may also appear as a result of an increase in salinity, chemical toxicity, oxidative stress or extreme temperature periods. Stresses happen every year in many crops all over the world, disrupting agriculture and food supply with terrible consequences.

To control stress conditions, plants are subjected to morphological, physiological, biochemical and molecular changes that adversely affect their growth and productivity.

With the aim of surviving, plants have developed through time several methods to withstand this lack of water. Since water stress reduces water content and turgor [1], plants close their stomatas, some pores in their leaves, to compensate these adverse effects which implies other issues like limiting gaseous exchange, reducing transpiration and arresting carbon assimilation rates. These events eventually entail a negative impact on mineral nutrition and a rise in leaves temperature that suppose a decrease in productivity and growth. The increase of stomatal resistance under stress levels indicates the efficiency of a species to conserve water and many plants have developed a huge resistance. Nevertheless, the majority of these plants are not crops and anyway, to put the plant through this state does not involve anything positive.

In fact, the average yields might be reduced by more than 50% because of hydric stresses [16]. This is due to the fact that water, which comprises 80-90% of the biomass of non-

[1] Turgor pressure is the force within the cell that pushes the plasma membrane against the cell wall. [15]

woody plants (like crops) is the primary molecule in all their physiological processes as it is the major means for transporting nutrients.

For this reason, having a good understanding of the water content in the crop could be considered as a primordial factor from an agricultural yield point of view since not only water save would be greater but also the productivity would rise considerably.

1.2 OUFTI-Next

Taking into account the previous arguments and since the land covered by a crop field is huge, one can think about a satellite to monitor the fields, it is here where OUFTI-Next makes its appearance.

This 3U[2] CubeSat, whose dimensions are 30cm x 10cm x 10cm (it could be a 6U, 30cm x 20cm x 10cm depending on the room required to install the dual band optical system), is a technological demonstrator conceived and developed by the Space Center of Liege a research center of the University of Liege. The satellite, designed from scratch by students on their last academic year under the supervision of professors and experts in the matter of the center, will provide information of changes in the temperature of the crop in order to get an early warming about water stress in the plants.

As plants are heated by the Sun, they release water through the stomatas on their leaves in the transpiration process, cooling themselves down. Nonetheless, if there is not enough water available in the surrounding, they close these pores to conserve water, increasing their temperature as already mentioned. They use these same pores to take up carbon dioxide from the atmosphere and do the photosynthesis (process through which they produce their food). If plants continue to experience water stress, they finally overheat or starve, and die. This must be specially avoided in irrigated agricultural fields. So that, monitoring the temperature can allow to know the water content.

The goal could be achieved in the visible spectrum, looking for regions where plants are so stressed that they have turned brown. However, this would be too late since it uses to mean that the plants are already or almost dead. For that reason, it is necessary to equip the spacecraft with an infrared camera in order to measure thermal IR radiation coming from the crop. So, plants struggling to stay cool and conserve water will be localized while they are still healthy enough to survive. Thanks to this data, agricultural managers will have time to act providing the quantity of water required.

Moreover, since we cannot avoid needing to eat and, besides, global population do not stop growing, it is compulsory a better track of how much water our crops need because of water save is becoming more and more vital.

This idea has already been introduced by NASA with ECOSTRESS (ECOsystem Spaceborne Thermal Radiometer Experiment on Space Station) [17]. Nevertheless, as it is said in its name, the system is installed in the Space Station thus, it only covers one orbit. If OUFTI-Next performs good results, owing to the facility that CubeSats show to form a constellation (low development cost), they could allow a global coverage in real time one day.

[2] 1U = 10cm x 10cm x 10cm

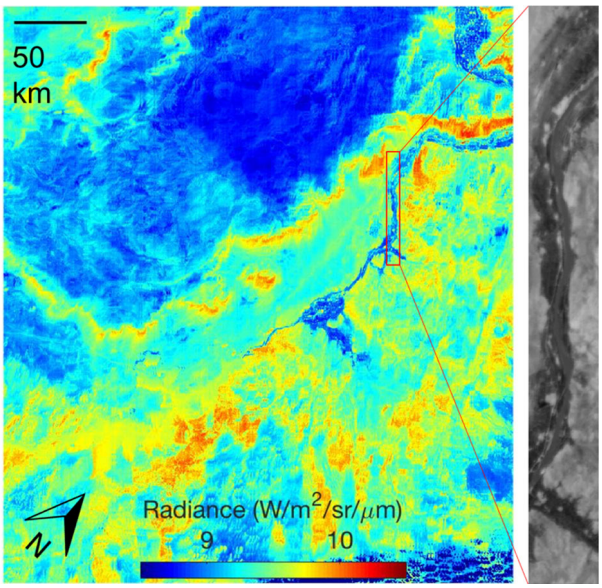

Figure 1.2: ECOSTRESS first light image. Taken the night of July 9 over Egypt. Yellow and red indicate higher temperatures. The marked red square is the River Nile [1].

1.3 Payload

The payload is the fundamental part of the spacecraft as it contains the devices that allow to fulfill the mission. If the payload does not work, although the satellite is still on orbit and with the rest of subsystems functioning, the mission cannot be carried out.

The payload can vary a lot depending on the mission, communication, surveillance, scientific goals, etc. In this case, the goal is the observation of the ground in IR. Therefore, a thermal camera conforms the payload needed. This camera is formed by an optical system that collects the electromagnetic radiation in form of photons that arrives to the satellite in the IR and by a detector that converts the electromagnetic power into an electronic signal and transfer the associated information to a device to produce the image.

The optical system is normally composed by lenses and/or mirrors, which adequate the rays to adapt the beam for the detector to work properly. In regards to the detector, it is formed by pixels, which are square portions that integrate a particular ray each and it is made from a semiconductor material, which is a material with an electrical conductivity that can drastically change with external stimulus, in this case, electromagnetic radiation.

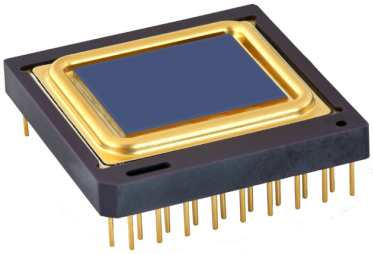

Figure 1.3: IR detector.

1.4 Previous work

After two years of development, OUFTI-Next is still in the design phase. Whereas OUFTI-1 took less time to be operative, the current mission is more complex and so, it requires more time. Observation is not an easy task, everything must be studied to the very small detail in order to get good results and images. The payload and the communication systems should be analysed very carefully, but, besides, there are several inputs to these two subsystems which have to be taken into account such as the orbit, the power, the thermal control, etc. everything is connected in a spacecraft.

This project was started with two master's thesis about the feasibility study of the payload in MWIR [18], in which a simple radiometric and signal to noise ratio analyses were performed, and about the platform [19], where the mission was assessed. After that, several works were documented studying the lenses (reflective, refractive and Fresnel lens [20], [21], [22]) and the system [23], but specially two master's theses are of relevant importance for the current document. The one related with the thermal control [3] and the one reporting the study of the orbit and attitude of the satellite [24].

From all these master's theses several outputs have been obtained. First of all, the dimensions of a CubeSat 3U must be introduced.

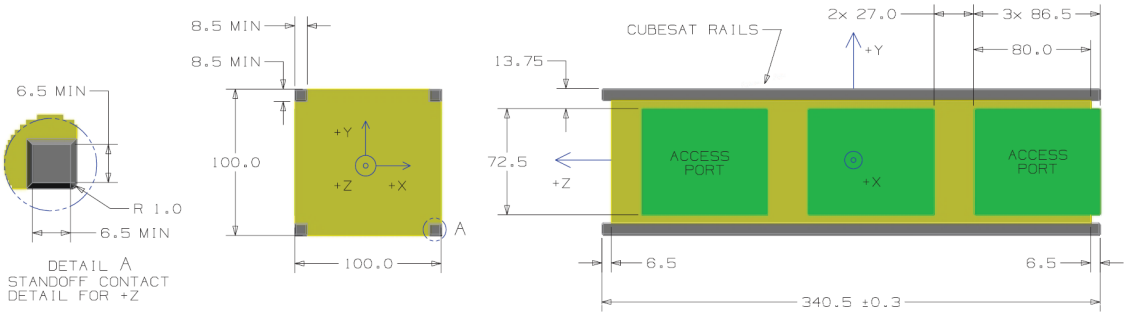

Figure 1.4: Dimensions [mm] of a 3U CubeSat according to the CubeSat Design Specification [2].

Next, numerous orbits were studied to get the most suitable one for this mission. Among all of the available orbits, two were analysed in detail, the orbit of the ISS and a SSO, nearly polar, at around 700 km. Each orbit presents its characteristics, advantages and inconveniences. SSO parameters can be designated in order to cover almost entirely both hemispheres. The main advantage of the SSO is the fact that the satellite passes over the same place at the same local time. Crops are producing their maximum transpiration at midday (max emission), between 12 and 14 h, therefore, a SSO represents a huge pro to perform the observation. However, it is not possible to study the diurnal cycle of the plants. Furthermore, the gain of lifetime on SSO could be up to 2 years, nevertheless, this is not very useful since OUFTI-Next is a technological demonstrator and so, with a few months operating should be sufficient to obtain the desired measures. On the other hand, with the ISS orbit, the cross time over a specific latitude is different at every passage, however, the ISS orbit is lower and therefore, the resolution achieved is better. Moreover, eclipse time are similar in both orbits ($\sim$ 30 min) [24]. Also, variables such as launch costs and revisit period must be taken into account for the final decision. For this study, SSO is considered.

About the resolution reached on these orbits, it was desired, at a first moment, to be around 25 m of spatial resolution. However, after a few calculations the GSD is expected to be around 100 m in MWIR. Through this document, it will be seen how depending on the band studied, the resolution can vary a lot.

Inside the spacecraft, 1.5U is destined to the payload along the Z axis in Figure 1.4, independently if the satellite is a 3U or a 6U CubeSat. Besides, the aperture of the payload is planned to be in the $-Z$ face regardless of the configuration of the solar panels, which are used to provide the quantity of power that the satellite needs, around the external structure, which is not precise yet. Three configurations have been studied depending on the amount of power required by the subsystems (Figure 1.5). The first configuration, known as body mounted or standard, is with the solar panels placed on faces $+X$, $+Y$ and $+Z$. If more power is required, the other two configurations are more useful, with four 3U solar panels mounted either on the top of the spacecraft, Face $+Z$, which is also covered, called cross configuration, or either two 3U deployable solar panels attached to face $+X$, which corresponds to table configuration.

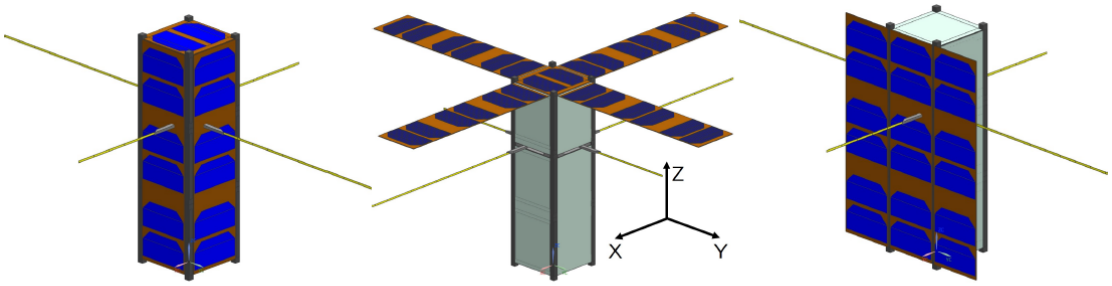

(a) Body Mounted (b) Cross (c) Table

Figure 1.5: OUFTI-Next's configurations [3].

In regards to the structure, it will be a modular 3U CubeSat structure supplied by ISIS [25]. This type of structure allows to collocate easily the spacecraft's components. The solar panels employed, in this case, are Ultra Triple Junction cells with 28% efficiency [26].

Besides, on the exterior of the satellite, two antennas will be placed. One is a GPS and the other one a S-band patch antenna. Communication with the satellite will be through UHF for commands (1.2 kpbs uplink) and VHF for telemetry (9.6 kpbs downlink). The S-band will be used to download images (1 Mbps) [24].

The interior of the satellite is composed by units, see Figure 1.6. The top of these units is where the PCB stack is located, which contains the circuit boards required for the spacecraft's bus. The upper component is the EPS-battery bundle that compound the power subsystem. After that, one can find the on-board computer. The lower two boards are the transceivers for the VHF/UHF and the S-band, respectively. Below the transceivers and for a standard configuration, the VHF/UHF dipole antenna module is positioned. The component over the payload is the ADCS module, which controls the attitude of the satellite, formed by three orthogonal reaction wheels and a star tracker.

One main input as it will be seen latter is the temperature of the payload. This value is obtained for the thermal control study realized in [3], where an analysis of the nominal temperatures of the different elements of the satellite with their uncertainties was carried out. It was concluded that the payload would be approximately between 200-260 K.

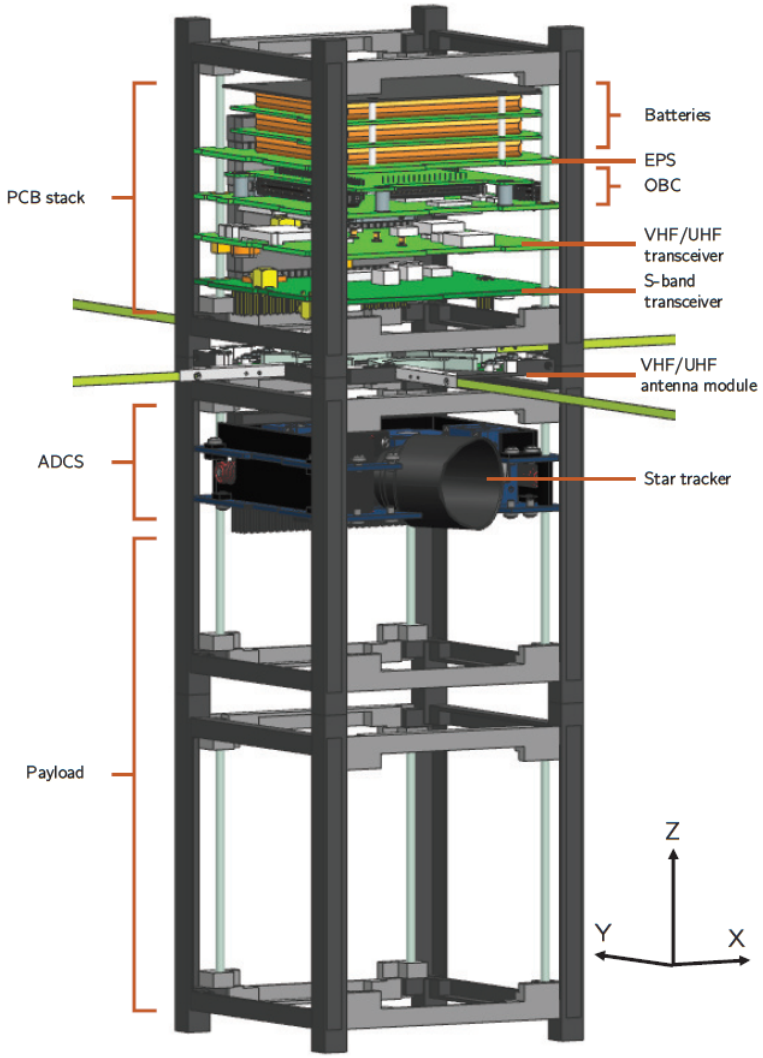

Figure 1.6: OUFTI-Next's interior [3].

For the thermal control of the optic system, two ideas have been considered. The first one consists of a passive cooling through a radiator which expels heat to the space. The second one is more complex and requires a considerable space of the payload, it includes a cryocooler to achieve a lower temperature in the camera's module.

Lastly, the satellite changes its attitude in function of the activity to perform. There are three modes or orientations. When the detector is taking the data, acquisition/imaging phase, the payload's face points towards nadir. After taking the images, it is necessary to download them with the S-band antenna, this is the communication phase. Therefore, this antenna, which is on face $-X$, must be pointing towards the Earth in this mode. The rest of the time, when the satellite is not carrying out any task, it is found in idle phase, which corresponds to a constant Sun pointing to charge the batteries with telemetry communication via UHF.

Moreover, it must be pointed that the radiometric budget and study of the signal and noise from [18], are taken as the basis or main reference of the current work.

2 | Objectives

This master's thesis reports the continuation of OUFTI-Next mission. After all considerations and work carried out in the previous section, the design team has decided to consider the option of turning the original MWIR mission into a dual band, so, MWIR and LWIR bands will be the main topic throughout this study.

Each band presents different characteristics, all of them will be seen in the current document. To introduce them, for example, MWIR produces a better optical resolution and the dimensions of the optics are smaller, but in LWIR it is possible to obtain a higher sensitivity and a clearer signal.

If this action is accomplished, it will procure several benefits. The availability of the optic system would be greater as there would be two bands to measure the temperature in crops. Moreover, introducing a LWIR camera would allow to obtain measures during the night cycle, because of the higher sensitivity of this band that allows to measure bodies at low temperature. In addition, thanks to the dual band, measures under different environmental conditions (humidity, haze, etc) could be performed.

However, some drawbacks will have to be overcome. The dual band observation means, a priori, more room required inside the payload to allocate the optics. Besides, it could also purport thermal issues that would have to be addressed.

To analyse the viability of this idea, the following patterns will be completed in this research:

- Establishment of the thermal and radiative concepts used in the model and statement of assumptions.
- Complete study of the radiometric budget for the fluxes that arrive to the spacecraft in both bands.
- Analysis of the optical dimensions and properties obtained depending on the band.
- Study of the Signal to Noise Ratio in function of the characteristics of the detector and the band.
- Representation and analysis of the actual output signal that the detector will produce as the convolute composition of the input signal coming from ground and the response time of the detector.
- Summary with the conclusions achieved and definition of new tasks for future development.

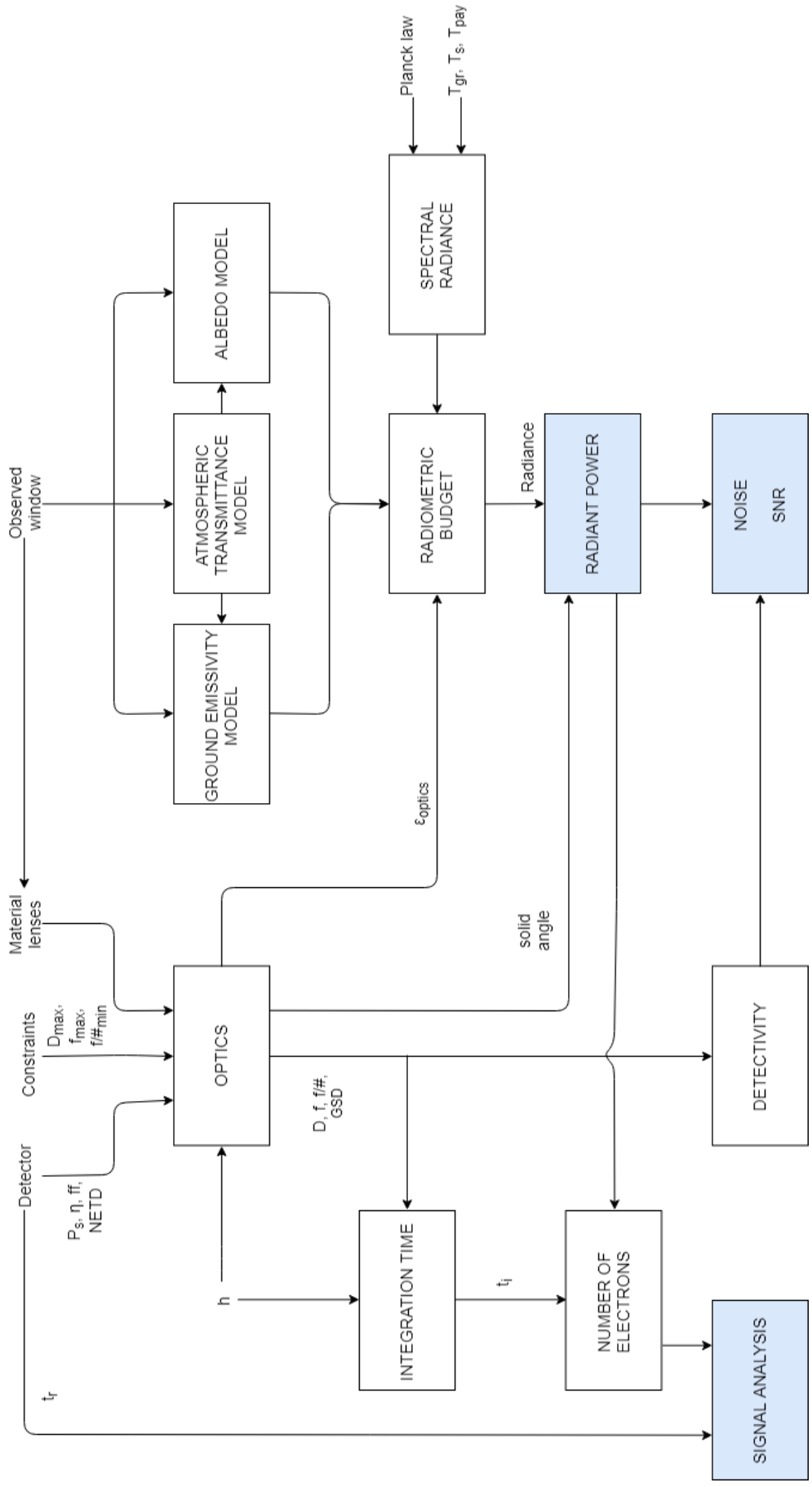

Figure 2.1: Block diagram of the model to perform.

3 Elementary concepts about radiation

In this chapter the main concepts about radiation from a theoretical point of view will be presented in order to understand and explain the physics behind the studied problem. Firstly, black body theory, which will be the basis of the whole radiative model, is introduced. After that, the characterization of materials from a radiative perspective is indicated.

3.1 Black body radiation

There are three modes through which it is possible to transfer thermal energy from one source to a receiver.

Convection is the study of heat transport processes effected by the flow of fluids [27]. It is a gravity-driven phenomena as heat is transferred by relative motion of portions of the heated body so that, in space, where planetary gravity is the only force acting on a body, with no contact forces, this transfer does not occur.

Conduction, in which heat passes through the substance of the body itself [28], will be paramount for the thermal design carried out by several master's thesis [3] and [29]. However, it will be ignored for this study.

Radiation, in which heat is directly transferred between distant elements by electromagnetic radiation hence, it is not required a medium between them to happen. The propagation can be conceived from two points of view: electromagnetic wave theory and quantum mechanics, being photons the carrier particles. The photon concept includes simplifications that allow the treatment of radiation in simple terms, even though, the equations from the electromagnetic theory, which envisages the radiation as waves that propagate with the speed of light in vacuum, are simpler and make it possible to solve engineering problems [4]. Both theories are important for this research.

To better explain heat transfer by radiation is crucial to introduce the concept of black body. A black body is a hypothetical object, which emits the maximum amount of energy on any given wavelength, this is fully determined by its temperature. It is a perfect emitter and absorber and provides a reference to express radiative characteristics of actual objects at a certain temperature.

The propagation of radiation coming from a black body can be measured in terms of the intensity, which is independent of the direction of the emission. It can be assumed that a black body radiates in a spherical distribution. The spectral radiance dependency with temperature and wavelength is obtained from Planck's equation:

$$L_e = \frac{2hc^2}{\lambda^5(e^{\frac{hc}{\lambda kT}} - 1)} \quad \left[\frac{W}{sr \cdot m^3}\right] \tag{3.1}$$

Where h is Planck's constant ($h = 6.626 \cdot 10^{-34}\ J \cdot s$), c is the speed of light ($c = 3 \cdot 10^8\ m/s$) and k is the Boltzmann's constant ($k = 1.38 \cdot 10^{-23}\ J/K$), just as a reminder $J = \frac{m^2 kg}{s^2}$.

EMR is spectral in nature, specified for a given frequency or wavelength, so that, it is usual to classify it as a function of this property (Fig 3.1).

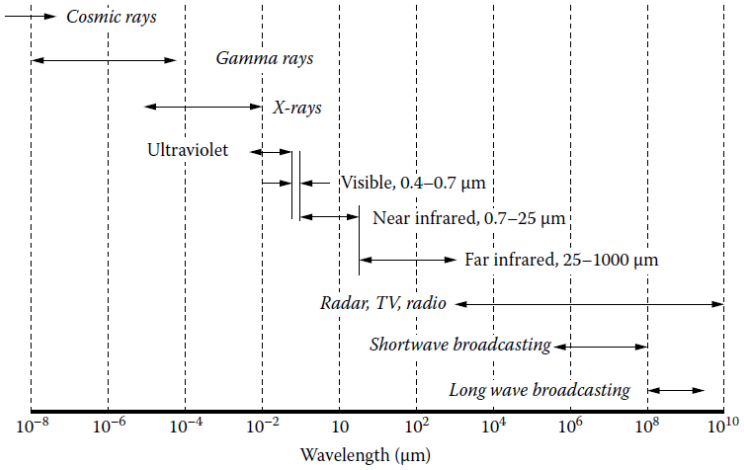

Figure 3.1: Spectrum of EMR in function of the wavelength [4].

The curve that represents Planck's equation shows a peak which variates in function of the temperature and shifts toward longer wavelengths as black body's temperature is reduced. The way this variation is produced can be determined by Wien's displacement law, which comes from the differentiation of Equation 3.1 with respect to λT:

$$\lambda_{max} T = \frac{\frac{hc}{k}}{5(1 - e^{-\frac{\frac{hc}{k}}{\lambda_{max} T}})} \longrightarrow \lambda_{max} T = 2898\ \mu m \cdot K \tag{3.2}$$

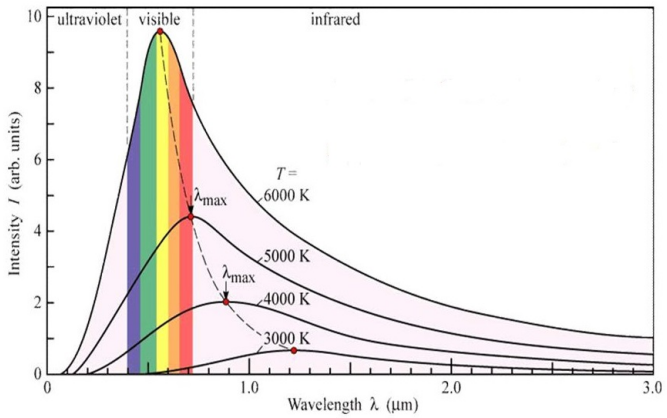

Figure 3.2: Wien's displacement law representation

This effect, appreciated in Figure 3.2, allows to conclude two statements. Firstly, the peak produced by the radiation of the Sun, considered as a black body at a temperature of 5800 K, is in the visible spectrum, around 0.5 μm, however, its radiation extends until the IR before being negligible. In addition, the peak of radiation emitted from a black body at around 300 K, such as the Earth can be considered, is found in the IR, around 9-10 μm. This will have its relevance, as it will be showed in the next chapter.

3.2 Radiometric properties

When a surface or medium receives an incident radiant flux, three processes occur: absorption, reflection (scattered or unscattered) and transmission, which are characterized by three ratios with respect to the incident radiation. All of them are normally dependent of the wavelength (spectral properties), although they can also be presented as weighted by a source function [30].

Transmittance, τ, is the fraction of transmitted power. Transmission is the process by which part of incident power is transmitted or passes through a surface.

Reflectance, ρ, is the ratio of reflected power. Reflection is the process produced when part of the radiant flux is returned into the same hemisphere from which it arrived. Reflection can be specular, if each ray is reflected with the same angle to the surface normal as the incident ray and in the same plane, but on the opposing side of the surface normal, diffuse, if the rays are scattered at many angles to the surface normal or a combination of both.

Absorptance, α, is the ratio of absorbed power. Absorption is the way by which a fraction of the incident radiation stays in the medium and is transformed into other type of energy, usually into heat.

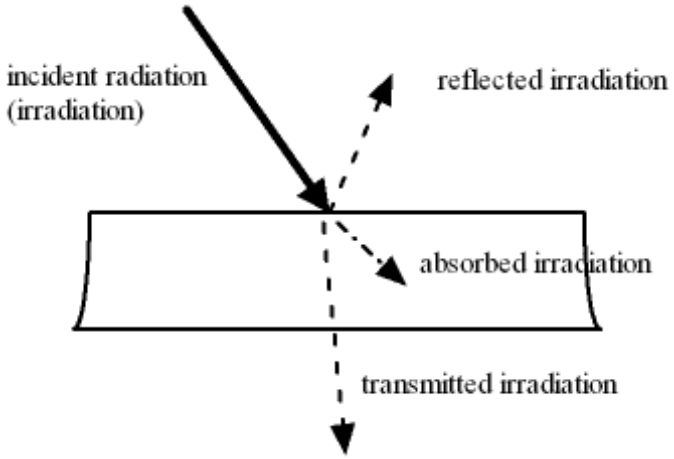

Figure 3.3: Radiative processes of a beam through a surface

Radiative properties of actual materials are mainly described by these three ratios. Since energy must be conserved, the sum of transmissivity, reflectivity and absorptivity of radiant flux that crosses a surface has to be equal to 1:

$$\tau + \rho + \alpha = 1 \tag{3.3}$$

It might be useful for any optical material with very low reflectivity to link the internal transmittance with its absorption coefficient, neglecting the reflectance losses. This can be done through Lambert-Bouguer-Beer law:

$$\tau_\lambda = e^{-\alpha'_\lambda d} \tag{3.4}$$

Where α'_λ is the spectral absorption coefficient, normally expressed in cm^{-1} at the respective wavelength and d is the thickness of the material. The product of this two variables is usually called optical thickness.

As one might observe, the radiative properties that have been seen until this moment are all related with the incident radiant flux, nevertheless, bodies with a temperature above 0 K, hence all real objects, radiate, so emission must also be taken into account to study radiation.

Emissivity, ε, is defined as the ratio of the radiant flux emitted by a body to that of a black body at the same temperature [31]. It can be assumed as the capability for thermal radiation by an object. The values for emissivity range between 0, for a body at absolute zero, and 1 for a black body. Moreover, this characteristic depends on the wavelength and the direction but, when the radiation emitted by an object is considered as independent of the wavelength, the material is often called a gray body.

Finally, emissivity is linked to earlier properties through absorptivity in Kirchhoff's law:

$$\alpha_{\lambda,\theta} = \varepsilon_{\lambda,\theta} \tag{3.5}$$

4 | Radiometric budget

The radiometric budget is a key parameter to know the signal that the satellite receives and from which source it comes. What is wanted to measure is the IR radiation of the crops in order to obtain their temperature, the rest of signals are perturbing the desired one since the detector is not able to discriminate the source. Hence, a study of the spectral radiance that the satellite perceives from each source is essential to know which waveband is more feasible to fulfill the mission.

This chapter dives in the radiometric budget of the satellite. The research starts with a presentation of the thermal infrared spectrum, subdivided in MWIR and LWIR bands. Next, the environment surrounding the spacecraft will be assessed, introducing the fluxes that could reach the detector and separating them in function of their origin. Finally, after the radiometric budget analysis, a comparison between the components involved is yielded.

4.1 Thermal infrared

The entire infrared spectrum covers the range from 0.7 μm, where red visible light is found, up to 1 mm, where radar waves start. It is subdivided in five main bands: Near-infrared (0.75-1.4 μm) Short-Wavelength Infrared (1.4-3 μm), Mid-Wavelength Infrared (3-8 μm), Long-Wavelength Infrared (8-15 μm) and Far infrared (15-1000 μm) [32].

Although each band shows its own advantages and it is useful to carry out a precise study for a particular target, in this project the loupe will be placed on both, MWIR and LWIR. These two bands compose the thermal infrared, in which the temperature of an object can be derived from its thermal emission.

A comparison between the two bands could be useful to appreciate the advantages and drawbacks of each:

About MWIR, it must be outlined that diffraction effects have less influence and the detector is less perturbed by satellite's own radiation, a very relevant issue. In addition, clarity (contrast) and stability (drift) are better [33]. Besides, for the same optics it is possible to work with lower pixel size and obtain lower GSD. However, the detector could pose some issues depending on the type implemented, photodetector or bolometer. If the first one is employed the detector will need to be cooled down at very low temperature, between 150 K and 90 K, something impossible for a passive cooling so that, an active cooling system would be required which is not currently planned for room reasons.

On the other hand, LWIR systems perform better at lower ambient temperatures. For that reason, it can be employed during night cycle, where plants are not doing the photosynthesis and present a lower temperature. It also operates better at lower relative humidities and under worse environmental conditions (fog and dust). Relative humidity is the ratio of the partial pressure of water vapor to the equilibrium vapor pressure of water at a given temperature [31]. Therefore, in cool air the same amount of water vapor results in higher RH than in warm air. What is more, the cost of LWIR cameras is much lower (between 3 and 4 times) and they do not require a cooling system to operate.

4.2 Fluxes

The radiation to which a satellite is exposed varies highly depending on the mission. A spacecraft orbiting the Earth, like OUFTI-Next, experiences an environment completely different from the one of an interplanetary orbiter and evaluating it, is a paramount point for the adequate development of the mission.

The main goal is to obtain the radiant flux from the crop (nominal or scientific flux) that arrives to the detector, but also the radiant flux from other sources that affect the signal received from the first one. So, only the acquisition phase will be analyzed. For this project, several sources of radiation are thought to influence in the radiometric budget.

Firstly, one can think about the direct radiation of the main emitter of the solar system, the Sun, a black body emitting at 5800 K [34]. Although Sun's peak of radiation is found in the visible range, see Figure 4.1a, its thermal IR radiation is important enough to be considered. However, the detector will be only operating during acquisition phase, when the payload is pointing towards the Earth hence, it is expected that the detector will be barely affected by Sun's direct radiation, reason why this flux has been ignored.

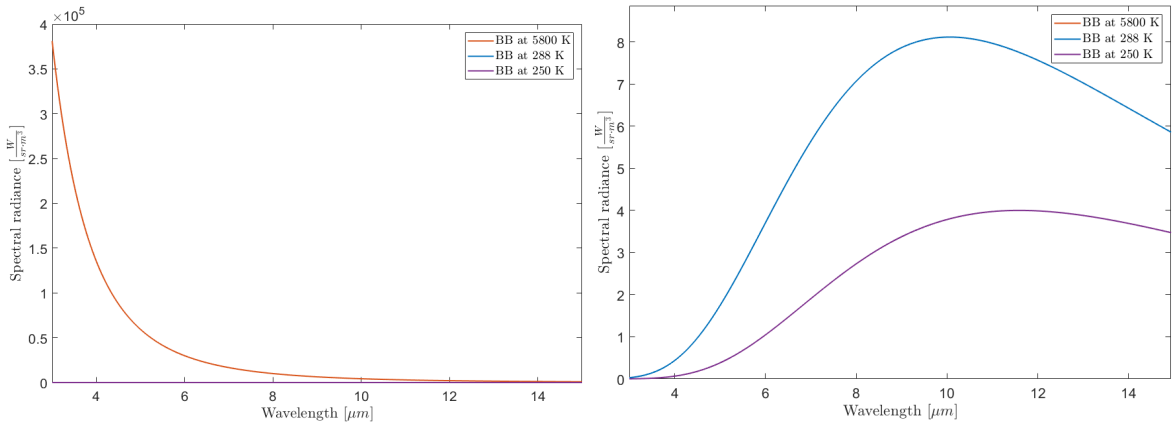

Figure 4.1: Figure *a* (left) shows the spectral radiance of a black body at different temperatures in function of the wavelength. Figure *b* (right) shows a zoomed version of this spectral radiance.

Nevertheless, Sun's radiation cannot be completely neglected, part of Sun's radiation that reaches the Earth is reflected back to the space by the atmosphere and the ground. This is called albedo and will have an effect on the observation due to the fact that if the power coming from this source is greater than the one from the crops, the taken image will be completely perturbed by this flux, impeding to know the state of the plants.

Of course, Earth's emission is paramount. Earth is usually conceived as a black body at a temperature around 255 K [35]. This value comes from Earth's surface temperature multiplied by a certain emissivity, which will depend on the surface material and the wavelength and it will be higher in IR as it will be demonstrated latter in this report. As one can observe from Figure 4.1b, the peak of radiation of a black body at 288 K is in the middle of the LWIR band, around 10 μm.

Next, the satellite itself is also an emitter that must be taken into account for the radiometric budget since its temperature is expected to be in the range 200-260 K [3].

Despite of observing in Figure 4.1 that Sun's term is much greater than the other two, it must be pointed that this is not exactly the albedo component. To be so, this curve, which represents what the Sun emits, ought to be multiplied by a factor that reproduces the amount of radiation from the Sun seen by the Earth and by the portion reflected by it.

Finally, Cosmic Microwave Background, which is electromagnetic radiation as a remnant from an early stage of the universe, considering a black body known as Deep Space at a temperature of 3 K is completely negligible in comparison with the rest of terms.

So, Figure 4.2 could be a good approximation of the fluxes considered.

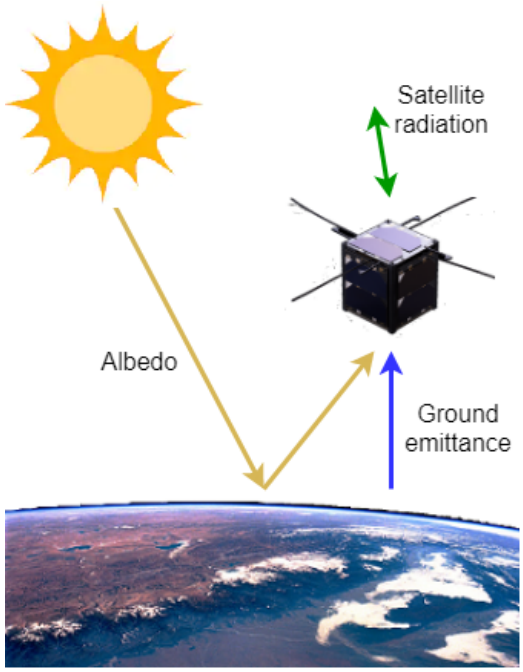

Figure 4.2: Incoming fluxes to the detector during acquisition phase.

It is possible to separate the fluxes from their origin. Albedo and Earth components will be analyzed as external fluxes to the satellite, whereas satellite's radiation as internal.

4.3 External radiometric budget

To study the external radiometric budget, a crucial feature must be characterized firstly, the atmospheric transmittance or fraction of radiation that the atmosphere allows to pass through.

4.3.1 Atmospheric transmittance

Earth's atmosphere is composed by several gases or constituents (Table 4.1) and a certain amount of water vapor, which govern the atmospheric transmission. Atomic gases (like Ar or Ne) and diatomic gases of the same atomic species (N_2 or O_2) do not absorb IR radiation in the thermal IR range. Nevertheless, molecules constituted by two or more different atomic species (NO, CO, CO_2 or H_2O) are capable of absorbing IR radiation [36].

Constituent	Symbol	Content of volume (%)
Nitrogen	N_2	78.084
Oxygen	O_2	20.948
Argon	Ar	0.934
Carbon dioxide	CO_2	0.0314
Neon	Ne	1.818×10^{-3}
Methane	CH_4	0.2×10^{-3}
Hydrogen	H_2	5×10^{-5}
Nitrogen monoxide	N_2O	5×10^{-5}
Ozone	O_3	7×10^{-6}

Table 4.1: Composition of dry air.

Because of these constituents, there are only several bands available for the thermal infrared in which observation can be performed since at certain wavelengths the atmosphere becomes completely opaque to IR radiation.

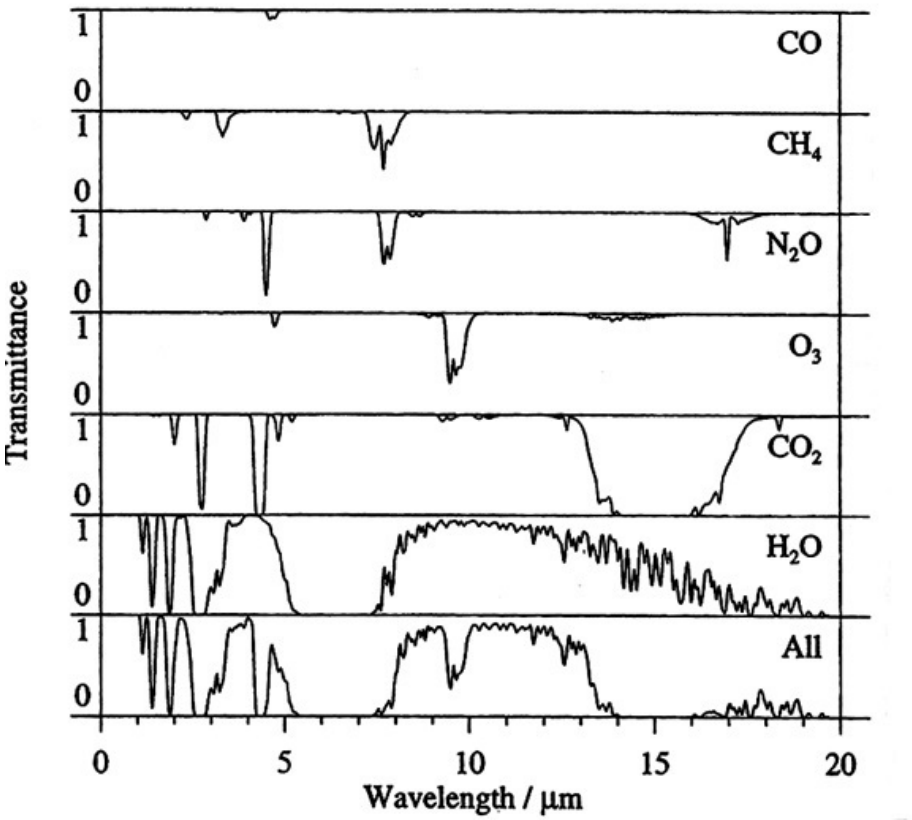

Figure 4.3: Absorption IR bands of the different constituents of the atmosphere.

It is possible to observe in Figure 4.3 that the constituent which more affects the atmospheric transmittance is H_2O. It presents two main absorption bands, one between 2.7-3.3 μm, separating SWIR from MWIR and the other one, which separates MWIR from LWIR, between 5.5-7.5 μm. The first one is also produced by the absorption of CO_2.

Another important absorption band can be found between 3.6-4.2 μm produced by two molecules, N_2O and CO_2. CO_2 also results in a big absorption band beyond 14 μm, while N_2O with CH_4 impede transmission after H_2O second gap, up to 8μm. Finally, O_3 absorption is important enough to generate a considerable gap in LWIR, around 9.5 μm.

In order to apply this knowledge to the study it is necessary to develop a model of the atmospheric transmittance. This model is implemented in Matlab, based on observations obtained at the Gemini Observatory [37].

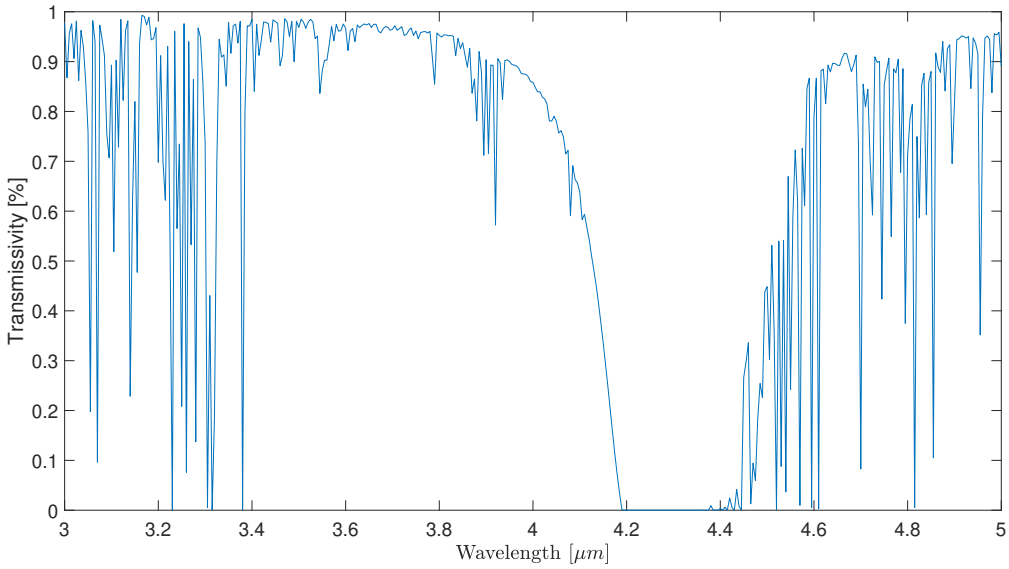

Figure 4.4: Atmospheric transmittance in MWIR [5].

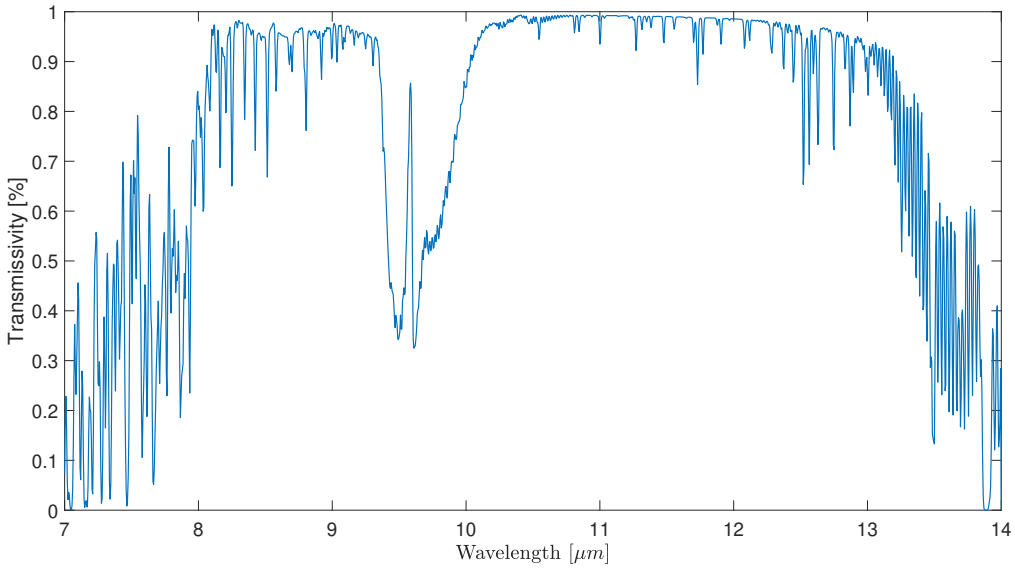

Figure 4.5: Atmospheric transmittance in LWIR [5].

One aspect must be distinguished before commenting these graphs. Transmission depends on the concentration of gas species. Although concentrations are constant for the majority of gases, water vapor concentration can greatly vary spatially and temporally, so its value must be clearly defined.

The results in Figure 4.4 and Figure 4.5 are obtained from Mauna Kea Observatory (Hawaii), one of the two observatories coordinated by Gemini association, with a precision of 5 nm, for a water vapor column of 1.0 mm and an air mass of 1.0.

The air mass coefficient defines the direct optical path length through the atmosphere, expressed as a ratio relative to the path length vertically upwards at the zenith [38]. As the satellite is thought to take images of the ground looking towards nadir, an air mass of 1 is considered. This value corresponds to the spectrum travelling through the atmosphere to sea level directly vertical, known as AM1.

For its part, water vapor column is a measure of the total gaseous water contained in a vertical column of atmosphere. This value should not be mistaken with relative humidity, which is the amount of water vapor in air relative to the amount of water vapor the air is capable of holding [39]. A value of 1 mm has been chosen arbitrarily.

Vertical transmission has values below 100% not only due to absorption losses but also due to scattering. When the particles are small relative to the wavelength, scattering fulfills the equation:

$$\sigma \propto \frac{a}{\lambda^4} \tag{4.1}$$

Where a is the particle size [40]. This is called Rayleigh scattering. So, there are several particles that affect transmission because of this effect. The molecules that conform the atmospheric gases which have a small size, around 1 Å [1] [41], provoke the blue colour in the sky, but their produced scattering show a rapid falloff as the wavelength increases. Also, different type of aerosols, not considered in the model, such as smoke, fog or dust, included in a major group, haze particles with a size around 0.1 μm, which perturb IR image, although it still enhances the results obtained in VIS. Due to the greater wavelength in LWIR, this band achieves better results than MWIR under bad weather conditions as the ones just mentioned. Whereas MWIR outperforms LWIR in high humidity conditions.

Moreover, it must be pointed that the model does not include the effect of clouds in transmission, which are opaque objects in the IR that could completely hide the surface of the Earth and therefore, the crop. This event is caused by scattering once again, since cloud droplets are large enough particles to affect IR wavelengths, around 10 μm. So that, it is considered a clear sky for the calculations.

4.3.2 Albedo component

Once the atmospheric model is well determined it is possible to start with the first component of the radiometric budget, the one that accounts Sun's radiation reflected by the Earth. As it has already been commented, Sun is a black body at 5800 K. Therefore, using Planck's

[1] $1\ \text{Å} = 10^{-10}\ \text{m}$

equation (Equation 3.1) one obtains the spectral radiance represented in Figure 4.1. This curve represents the amount of power along the spectrum per unit of area and steradian.

Before continuing, it is necessary to introduce the concept of solid angle and steradian. If one considers spectral radiance, which spreads homogeneously in a sphere, propagating along a given direction and inciting on a small control volume, this energy would be confined in a conical region, the solid angle, whose vertex would be the radiative source [4]. The solid angle defines the quantity of the visual field occupied by an object.

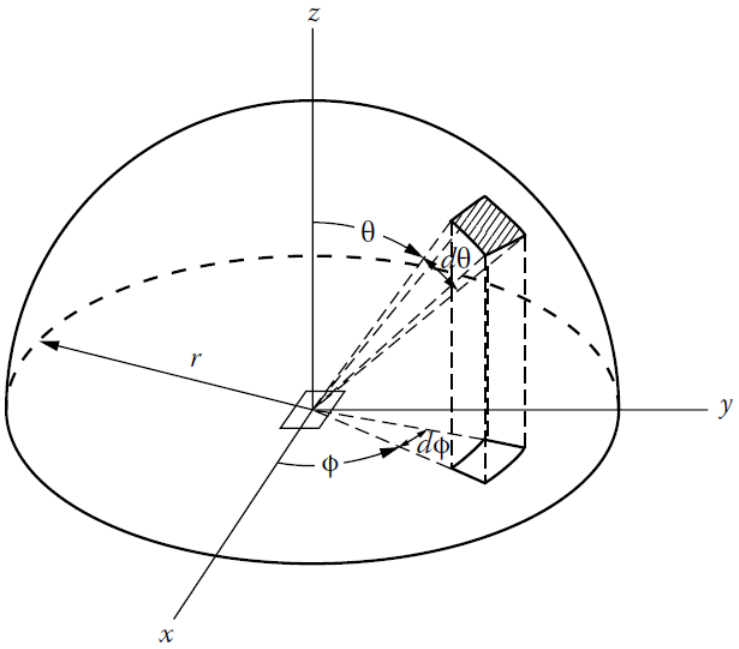

Figure 4.6: Solid angle in an hemisphere for a given direction.

The solid angle is similar to a planar angle, but is given in three dimensional space and its unit is the steradian, *sr*, defined as the solid angle that, having its vertex in the centre of a sphere, cuts off an area of the surface of the sphere equal to that of a square with sides of length equal to the radius of the sphere [42]. Based on Figure 4.6, the integral over all angles of a hemisphere yields:

$$\int\int d\Theta = \int_{\theta=0}^{\pi/2}\int_{\phi=0}^{2\pi} \sin\theta d\theta d\phi = 2\pi \ [sr] \tag{4.2}$$

In order to apply this concept in the current problem, the distance Sun-Earth is big enough to consider the Earth as a point in space, so that it is possible to calculate the solid angle between the Sun and the Earth knowing the distance Sun-Earth, 149,597,870 km, and Sun's radius, 695,510 km.

$$\theta = 2\sin^{-1}\left(\frac{R_{sun}}{d_{sun-earth}}\right) = 0.5328° \tag{4.3}$$

$$\Theta = 2\pi\left(1 - cos\frac{\theta}{2}\right) = 6.7906 \times 10^{-5}\ sr \tag{4.4}$$

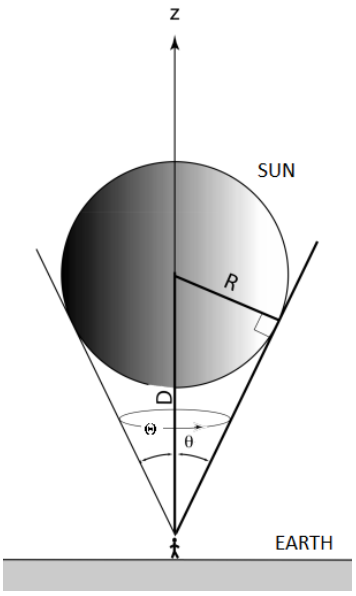

Figure 4.7: Solid angle Earth-Sun.

Now, if one multiplies the spectral radiance of the Sun by this value, the spectral irradiance that reaches the top of Earth's atmosphere is yielded. In the model, the slight daily and annual variations due to Earth's rotation around its own axis and the star are discarded. So, the solid angle Earth-Sun is assumed to remain constant.

In order to reach the ground, the irradiance must pass through the atmosphere where, applying the atmospheric model, only a part of it is transmitted to the ground. That portion of radiation arriving to the surface suffers the same processes, but with a different quantity, a part of it is transmitted, another reflected and another absorbed. The interesting irradiance is the portion reflected back by the Earth. This quantity is estimated through the albedo, as already mentioned. However, albedo is not an easy variable to estimate. Though a global average is a value of 0.3, it can vary a lot depending on the surface reached, but also depending on the wavelength (up to 0.6 for ice in VIS [43]).

To approximate the albedo it has been used the data from the ECOSTRESS Spectral Library [44], which is a compilation of over 2400 spectra of natural and man made materials developed as part of the ASTER and ECOSTRESS projects by the JPL, JHU and USGS-Reston. ECOSTRESS Spectral Library groups the materials from their origin. There are 7 categories and from each, several representative materials have been chosen for the study:

- Man-made materials: construction concrete, black gloss paint, pine wood, construction asphalt and aluminium roof.
- Rock: dolomite, carbonate, limestone, quartzite, siltstone and sandstone.
- Non-photosynthetic vegetation: misc leaf litter, misc grass litter, barks and branches.
- Soil[2]: reddish and brown alfisols (silty loam), entisol (sand) and mollisol (silty clay).
- Water: water, ice and snow.
- Vegetation: grass/crops, shrubs and trees.

[2]These soils were chosen according to suitability for crops [45]

The curves that represent the reflectivity of these surfaces can be found in Appendix A. To apply them to the model, two approaches have been carried out. The first one was simply computing the average albedo of all the studied materials. The second one was to apply a weight factor model. This model consists on giving values to each of the 7 groups, but the different types of vegetation that are separated, in function of their importance, which is defined by the amount of time that the satellite is expected to observe these materials. Following this method, the order of importance and the weight factors would be:

$$Crops = Shrubs > Water = Trees = Soils = Rocks = Non-living\ plants > Man\ made$$

Crops	1	2	2	2	2	2	3																						14/75
Shrubs	1							2	2	2	2	2	3																14/75
Water		1						1						1	1	1	1	2											8/75
Trees			1						1					1					1	1	1	2							8/75
Soils				1						1					1				1				1	1	2				8/75
Rocks					1						1					1				1			1			1	2		8/75
Non-living						1						1					1				1			1		1		2	8/75
Man-made							1						1					1				1			1		1	1	7/75

Table 4.2: Weight factors of the different materials studied in albedo.

Crops and shrubs are expected to be the elements that the satellite perceive most of the time and so, they have the major relative importance. Man made materials are not thought to be normally present, reason why the have the less relative importance. In Table 4.2 the process is as follows. Each element is compared with the rest. If it has the same importance as the other it sums a 1, if it is more important it sums a 2 and if it is much more important it sums a 3 while the compared one sums always 1. After performing this with all materials, the numbers are summed. The weight factor (right column) of each element is obtained by dividing its corresponding sum per the total sum of all materials. Eventually, each weight factor has to be multiplied by the reflectivity of the corresponding material.

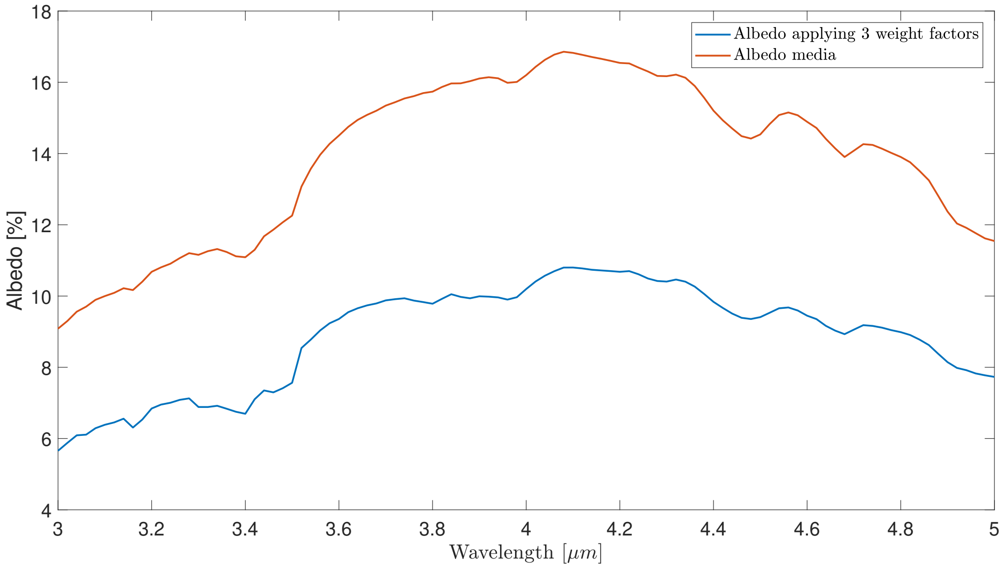

Figure 4.8: Albedo vs wavelength models in MWIR.

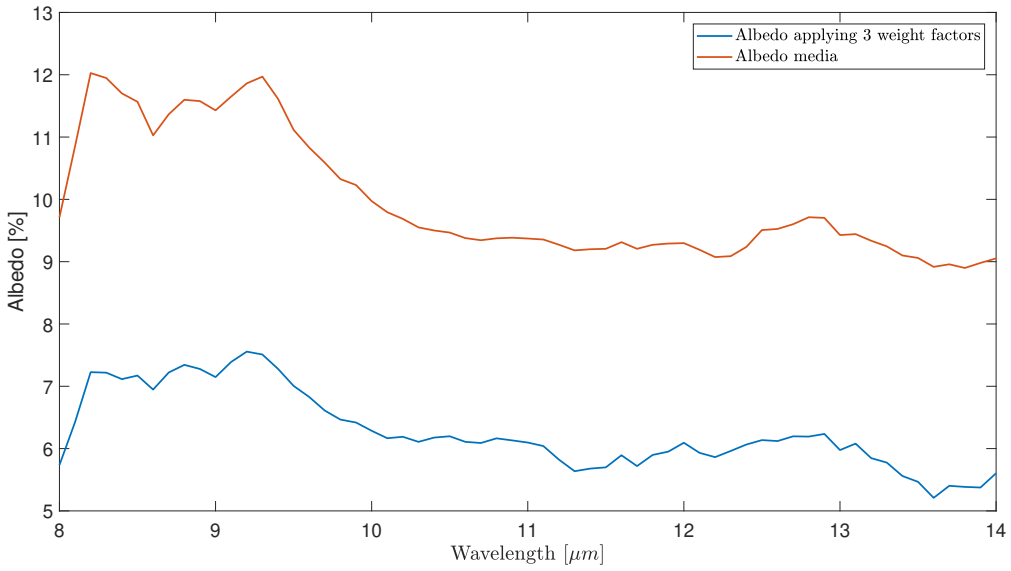

Figure 4.9: Albedo vs wavelength models in LWIR.

As one can notice in Figure 4.8 and Figure 4.9 the albedo of the Earth in IR is around the order of 0.1. The curves described by the two models show a similar shape, the difference lies in the values, being higher for the first approximation. This is due to the fact that vegetation presents lower reflectivity than the rest of materials, especially compared with man-made materials. Despite being the first approach more restrictive as it represents the worst case, it is thought that the second one depicts in a better way the real situation of the spacecraft and it will be implemented in the calculations.

It should be outlined just for scientific purposes that against what could be considered as a popular thought, frost and snow do not show a super high reflectivity in IR. It is true that their albedo is around 0.8 in the VIS domain, but it decreases rapidly as the wavelength rises, see Figure 4.10.

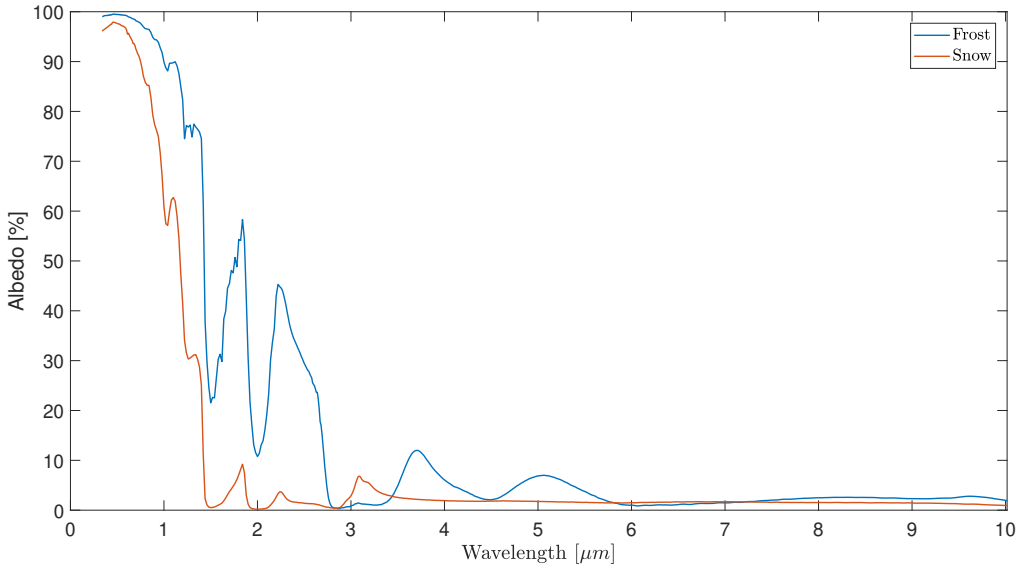

Figure 4.10: Albedo vs wavelength for snow and frost.

To reach the top of the atmosphere the irradiance reflected by the ground needs to transverse again the atmospheric layer, with the consequent loss of irradiance that this entails. Assuming that only half of the Earth is receiving sunlight, while the other hemisphere is at night, the irradiance must by divided by the solid angle of an hemisphere (Equation 4.2), arriving to the following equation that describes the spectral radiance at the top of the atmosphere produced by Earth's albedo.

$$L_{alb} = \frac{L_e(\lambda, T_{sun}) \cdot \tau^2(\lambda) \cdot a(\lambda) \cdot \Theta}{2\pi} \tag{4.5}$$

In the model, it has been considered clear sky again. However, albedo of a surface is a function of cloud cover. This occurs because of the same reason why IR cannot pass through clouds. Cloud droplets scatter radiation from the Sun in all directions and an important part of it is reflected back to space. In fact, up to 70% out of the total that the Earth reflects it comes from the clouds [46]. Normally, the diffuse component due to solar reflection from clouds is added to the clear sky albedos for unshaded surface. Contribution of clouds to albedo is represented in Figure 4.11 as a function of the optical thickness of the cloud layer, which can be approximated as twice the sum of the cross-sectional area of all drops in a unit area column [47].

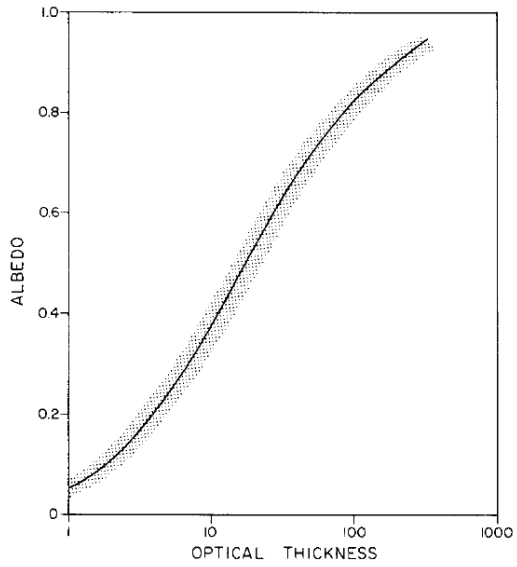

Figure 4.11: Cloud albedo vs optical thickness.

The albedo rises with the optical thickness, something expected as if there is more cloud, there are more droplets for the particles to collide with. Nonetheless, as it was commented before, clouds are opaque elements in the IR range, so there is no other alternative but making the observations when there are no clouds.

Furthermore, there have been dismissed another factors that might affect this flux. Firstly, rainfall can change the albedo, especially accumulations of less than 1.0 cm, which can produce up to 30% of variation in LWIR [48]. Eventually, aerosol effects have been again not considered, nevertheless, their atmospheric heating rate has been found to be many times larger than that due to CO_2 and about one-third that contributed by water vapor. It reduces downward solar irradiance by 9% and improves the diffuse solar fluxes at the surface by a factor 3 to 10 [49].

4.3.3 Ground component

Unlike the Sun, Earth's emission only have relevance in the IR domain, that is the reason why it cannot be seen by the human eye and only special detector and cameras are able to perceive it. Earth can be conceived also as a black body radiating at a certain temperature, the temperature of the ground, which for the project will be varying between 270-310 K. So, using again Planck's equation (Equation 3.1), one would obtain the spectral radiance of the Earth.

Moreover, Earth is not a perfect black body, it only emits with a certain unitless emissivity. The value of this emissivity depends on the surface and it must be calculated if one desires to know the true spectral radiance coming from Earth's ground emittance.

The emissivity of the majority of natural surfaces is between 0.6 and 1.0. Emissivities lower to 0.85 are only typical from deserts and semi-arid areas, while vegetation, water and ice use to have the higher emissivities, above 0.95 [50].

However, in order to get a precise model, approximating the whole emissivity by just one value could result not enough accurate. Instead, a piecewise function is applied, so, the emissivity of the ground turns into a wavelength-dependent function.

The different types of ground considered are the ones established by the IGBP as the global land cover types, there are 18 [51]. Though only a few will be interesting for the development of this research, the emissivity of the rest of surfaces can be found in Appendix B. In summary, the definitions of the cover lands matter of study are:

- Closed shrublands: Surface consists of shrub (evergreen or deciduous) coverage over 60% and vegetation with a height lower than 2 meters.
- Grasslands: Surface covered by herbaceous types. Tree and shrub are present in less than 10%.
- Permanent Wetlands: Surface consists of a permanent mixture of water and herbaceous or woody vegetation.
- Croplands: Surface composed by temporary crops followed by harvest and a bare soil period.
- Natural Vegetation Mosaics: Surface consists of a mixture of forest, shrublands, grasslands and croplands with none component comprising more than 60% of the landscape.

The following calculation will be computed considering cropland soil, though this could be changed whether the actual land viewed suits more with another cover land definition. Moreover, the same considerations made for the albedo component about clear sky are taken. Therefore, the equation that allows to calculate the spectral radiance coming from Earth's ground at the top of the atmosphere is:

$$L_{gr} = L_e(\lambda, T_{earth}) \cdot \tau(\lambda) \cdot \varepsilon_{gr}(\lambda) \tag{4.6}$$

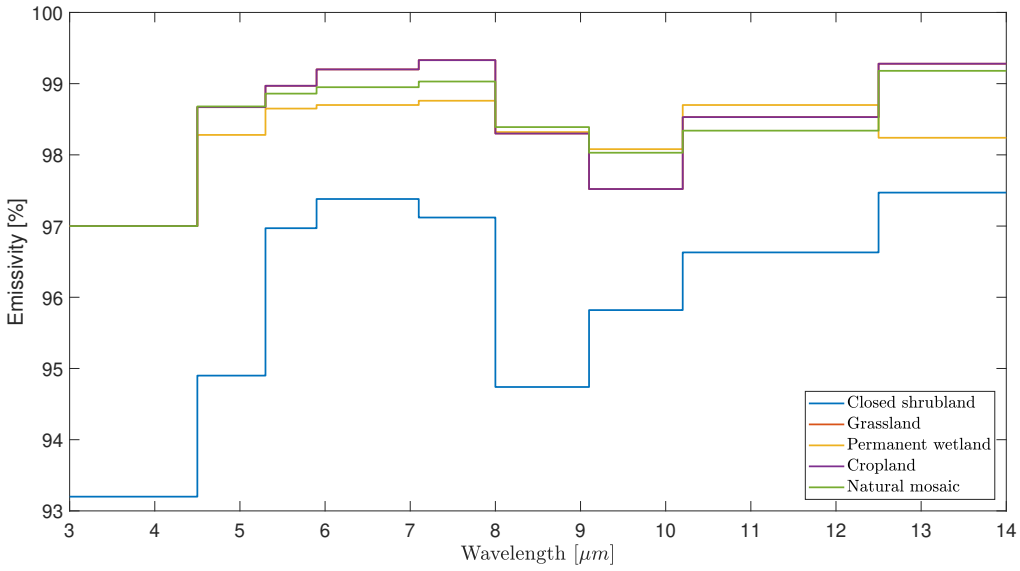

Figure 4.12: Emissivity vs wavelength for studied cover lands [6].

4.4 Internal radiometric budget

The internal radiometric budget is only due to the radiative flux coming from the satellite itself and so, it does not depend on the atmosphere.

4.4.1 Payload component

The spacecraft itself is also a radiator that cannot be lightly dismissed. The spectral radiance produced by the satellite as a black body can be again calculated from Planck's equation (Equation 3.1), multiplied by a certain emissivity. Based on previous works [3] and [29], the spacecraft is expected to have a temperature range between 200-260 K. The satellite will be approximated as a grey body, so its emissivity is independent of the wavelength.

To approach the flux that the detector perceives, the payload is assumed to be perfectly isolated from the rest of the satellite. So that the detector only sees the radiation coming through the payload aperture and none from the walls that surround the optic system, thanks to the coating applied. The type of coating was evaluated in [3], where it was decided to imply coated metal plates, in this case, aluminium coated with gold, achieving an emissivity of 0.02, considered as negligible in this study. This insulator was selected instead of the usual multi-layer insulation (MLI), since its emissivity would be approximately 0.1 and could cause contamination problems of outgassing because of the small dimensions of OUFTI-Next.

So, the radiative source from the satellite will only be the different lenses. In fact, what is called the payload aperture in Figure 4.13 is also a lens. Therefore it is essential to know their emissivity. To do so, it is paramount to define two properties of the lenses, the material and the thickness.

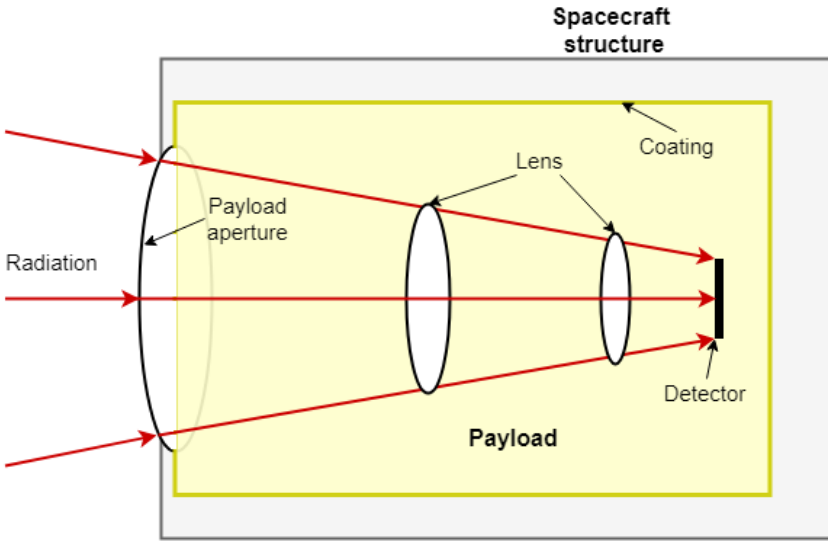

Figure 4.13: Payload scheme.

Thickness is expected to be between 5 and 10 mm [52]. For this study it will be supposed a 10 mm lens, as it represents the worst case. About the material employed a more in depth view is required.

There are several suitable materials for the lenses in the thermal IR. It exists a complete master's thesis discussing the theme of the optical materials [8]. Therefore, only the essential topics about them from a radiometric perspective, this is, to estimate their emissivity, are treated on this document.

Perhaps the most common optical material in IR is Germanium (Ge), which is a crystalline material that is able to operate in both MWIR and LWIR bands. Its major characteristic is the highest refractive index between all IR materials, which allows a great aberration control. The refractive index is the ratio of the speed of light in vacuum and the phase velocity of light in the medium, so it defines how fast light propagates through the material as it determines how much the path of light is bent when it enters the material, the higher the index, the more the rays are bent. Another very common crystalline material is Silicon (Si), it is characterized for showing a considerable reduction of transmissivity in LWIR, reason why it can only be used in MWIR [53]. Transmission of these two material in function of the wavelength is shown in Figure 4.14.

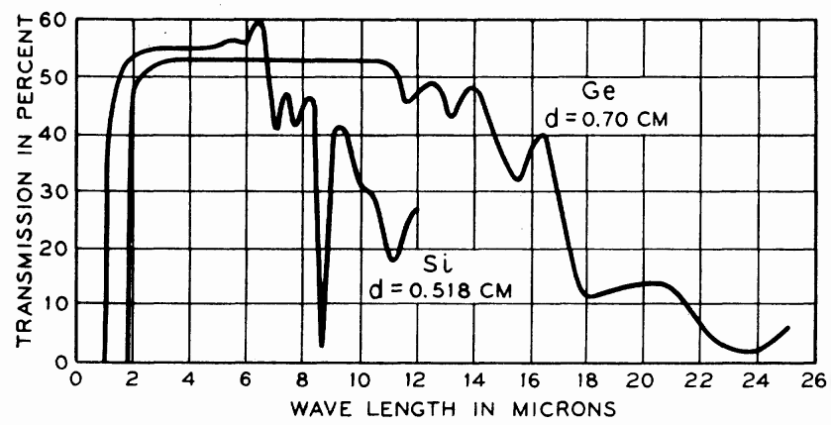

Figure 4.14: Transmission vs wavelength for Si and Ge, d is the thickness of the material [7].

Chalcogenide materials such as Zinc Sulfide (ZnS) and Zinc Selenide (ZnSe) are widely used. They are both employed in MWIR and LWIR bands and they have very similar properties. The main differences are that ZnSe has a higher refractive index and a lower structural strength and absorption coefficient [53].

Furthermore, IRG27, a material created by SCHOTT [54], based on a classic chalcogenide glass, arsenic trisulfide (As_2S_3), presents very interesting optical properties in thermal IR band, with a raw transmission about 0.65 [55]. In fact, this material is thought to compound the last lens of the optics system.

It is important to know that the transmission of raw materials, such as the one plotted in Figure 4.14, includes reflection losses. However, companies apply antireflective coatings (ARC) [3] to the lenses in order to obtain a significantly higher transmittance, reducing in most of the cases reflectivity to less than 1%. For that reason, it is possible to use Equation 3.4 to calculate the emissivity of the materials. Table 4.3 illustrates the most relevant mean optical properties of the materials studied.

Material	Refractive index	Absorption coefficient [cm^{-1}]		τ [%]		ε [%]	
		MWIR	LWIR	MWIR	LWIR	MWIR	LWIR
Ge	4	0.005 @ 4μm	0.027 @ 10.6μm 0.1 @ 12μm	0.995	0.973 0.905	0.005	0.027 0.095
Si	3.42	0.01 @ 3μm	1.5 @ 10.4μm	0.99	0.223	0.001	0.777
ZnS	2.25	0.02 @ 3.8μm	0.24 @ 10.6μm	0.98	0.787	0.02	0.213
ZnSe	2.4	0.0004 @ 3.8μm	0.0005 @ 10.6μm	0.9996	0.9995	0.0004	0.0005
IRG27	2.4	0.0151 @ 3μm 0.1381 @ 4μm 0.005 @ 5μm	0.0356 @ 8μm 0.947 @ 10μm 2.1371 @ 12μm	0.985 0.871 0.995	0.965 0.388 0.118	0.015 0.129 0.005	0.035 0.612 0.882

Table 4.3: Optical properties of IR materials [8] [9] [10] [11].

Regarding the optical properties of the materials, one can realize that, just from a radiometric point of view, for MWIR all the materials are suitable, although careful attention must be paid if finally IRG27 is implemented, as it reduces considerably its transmissivity at around 4 μm. On the other hand, for LWIR, only some materials can be used, Si (as it was advanced) and IRG27 are absolutely discarded as they can even be considered opaque in LWIR. The most interesting two for this band are Ge and ZnSe, however, they are both very expensive, specially ZnSe.

So, based on Table 4.3 results, which significantly varies with the wavelength and the material of the lenses, something not yet completely specified at this stage of the project, a conservative value of 0.1 for the emissivity of the payload will be taken. Knowing this value and the spectral radiance of the satellite as a black body it is possible to compute the internal flux radiated by the spacecraft to the detector.

$$L_{pl} = L_e(\lambda, T_{pl}) \cdot \varepsilon_{pl} \tag{4.7}$$

[3] More information about ARC in [56].

4.5 Comparison

After defining the assumptions and making the calculations for the different fluxes, it is possible to establish a comparison between them.

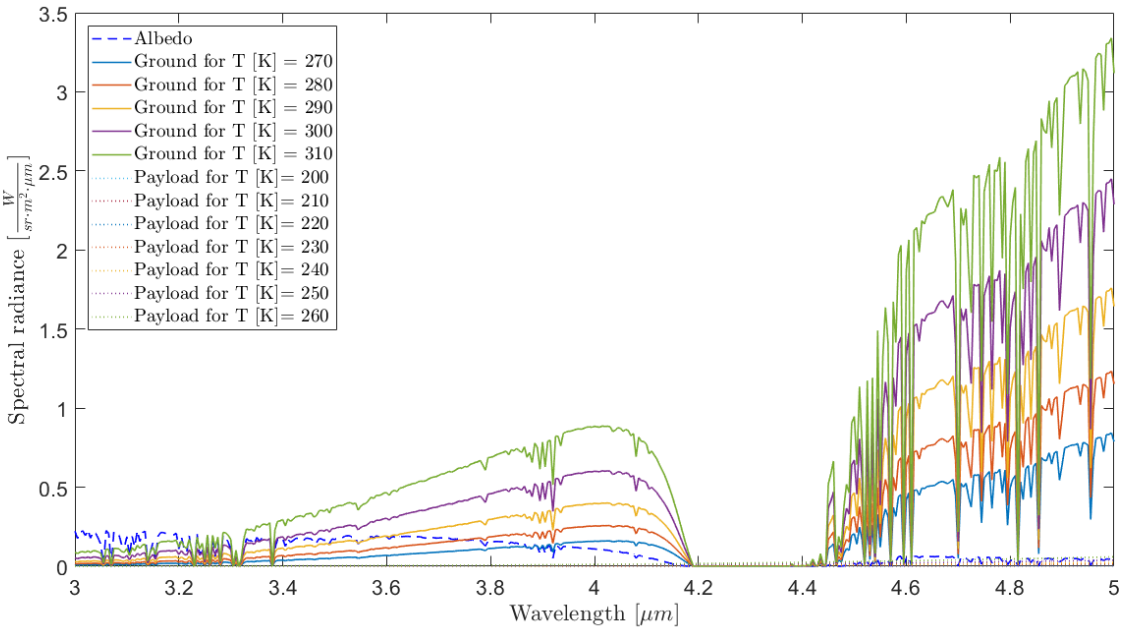

Figure 4.15: Spectral radiance of the three components vs wavelength in MWIR.

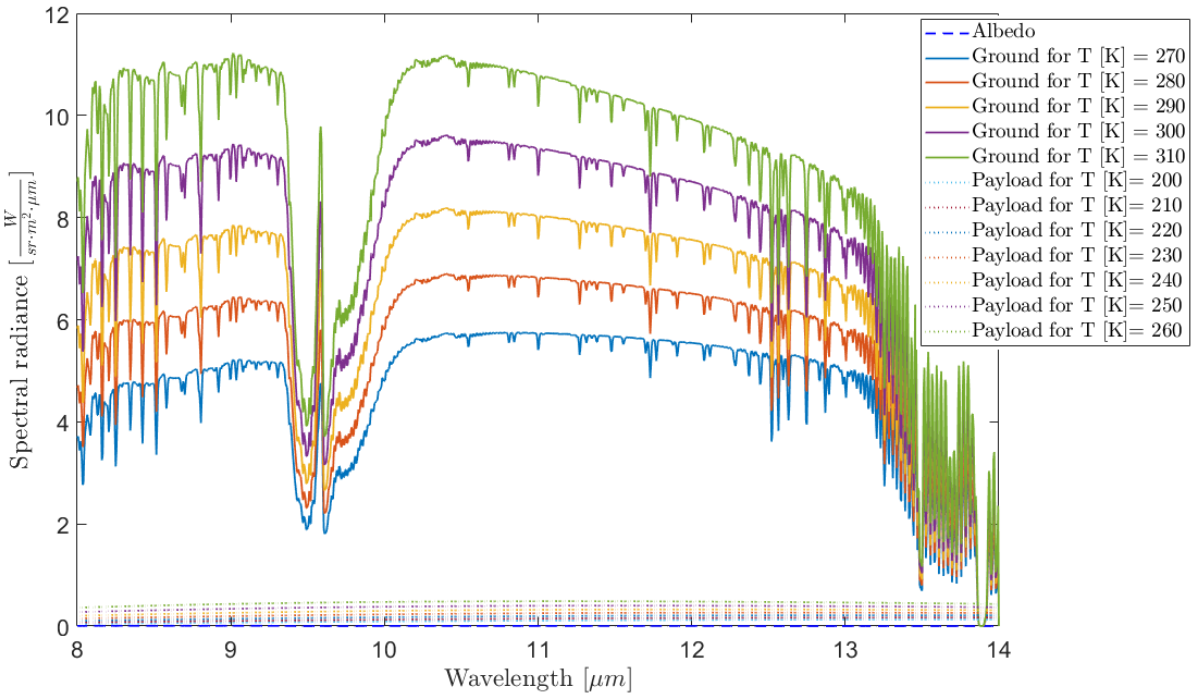

Figure 4.16: Spectral radiance of the three components vs wavelength in LWIR.

Hence, Figure 4.15 shows the flux radiated by the three components to space in MWIR band. It can be seen how the flux radiated by the satellite is negligible for the whole band in comparison with the other two. As one can notice, albedo component is predominant for the first wavelengths and, around 3.6 μm, ground emittance component starts to impose, increasing its value whereas the albedo decreases. There is a big gap due to the atmospheric transmission between 4.2-4.4 μm, after that, ground emittance component shows a significant increase while albedo is still decreasing. Therefore, for observation, it is feasible to define two bands, one for 3.6-4.2 μm, perturbed considerably by the albedo, and another one for 4.4-5 μm, where the signal received from the ground emittance will be cleaner.

On the other hand, Figure 4.16 represents the three radiative fluxes in LWIR band . In this case, albedo component is lower than payload's component, but they are still not enough important in comparison with ground emittance. Therefore, and this is a major benefit of LWIR band, despite existing a considerable decay due to the absorption in the atmosphere between 9 and 10 μm, LWIR band can fully cover (depending of the lenses) the study of Earth's surface from a radiometric perspective.

Comparing the spectral radiance coming from the ground component in MWIR and LWIR, it can be seen that in MWIR for a ground temperature of 290 K, for example, for the band between 3.6 and 4.2 μm is around 0.25 units, while between 4.4 and 5 μm is around 1 unit. However, for LWIR is around 6 units, much higher. Therefore the IR radiation of the crops will be greater in LWIR band, resulting in a better sensitivity. Moreover, the undesired signals are negligible in LWIR while in MWIR cannot be discarded as the albedo will perturb the images taken for observation below 4.2 μm.

Another important parameter to compare is the thermal contrast. It is defined as the ratio of the derivative of the radiance of the ground component with respect to the temperature to the radiance of the ground component [59]. The radiance is the integral of the spectral radiance with respect to the wavelength.

$$C = \frac{dL_{gr}(\lambda, T_{gr})/dT}{L_{gr}(\lambda, T_{gr})} \tag{4.8}$$

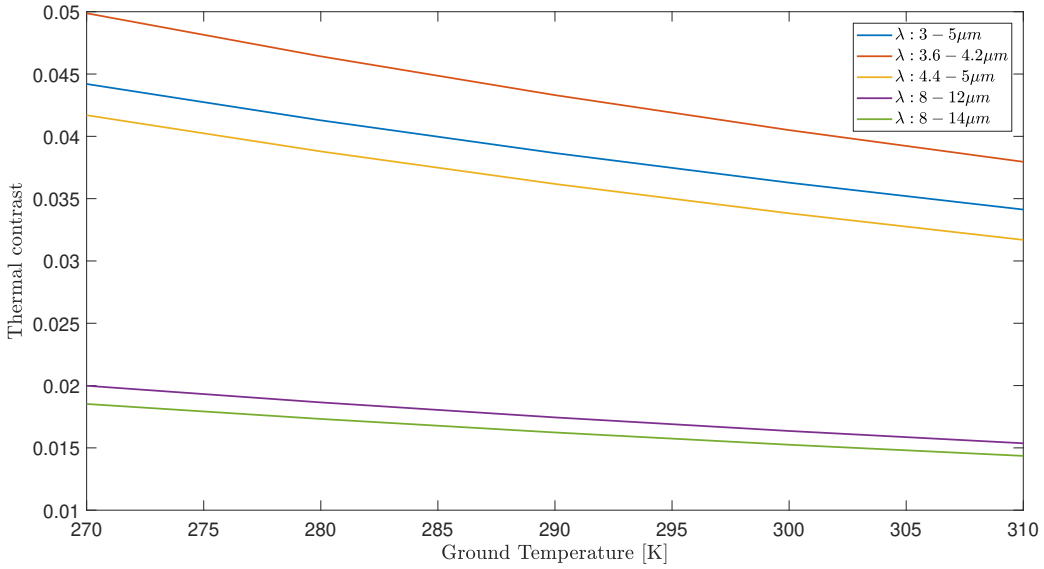

Figure 4.17: Spectral contrast in the MWIR and LWIR.

Due to the fact that a thermal image is produced from temperature variations, when the temperatures of a target and its background are very similar, detection becomes difficult since the sources can be confused. The thermal contrast determines the capability of detecting details.

As it can be seen in Figure 4.17. The contrast is much higher for MWIR bands. In fact, the band which shows the greatest contrast is one formed from 3.6 to 4.2 μm. For example, for a ground temperature of 290 K, the contrast is between 3.5-4.5%, while for LWIR the values are between 1.6-1.8% for the same ground temperature. In general, the contrast in MWIR is more than the double than in LWIR.

5 | Optical system

This chapter analyses the optical system for both, MWIR and LWIR. To do so, it is firstly necessary to introduce some concepts and equations that will govern the problem. After that, a parametric study of the optics will be performed, concluding with a comparison between the two bands.

5.1 Introduction

The optics are very attached to the detector. One depends closely on the other. Changing the detector it means the obligation of varying the whole optic system in order to obtain a suitable observation.

The goal of the optical system is to adequately collect the power that reaches the detector, which will then convert that power into an electric signal and, eventually, with that signal an image will be produced. This subsystem could be considered as the most important of the satellite, since if it malfunctions, no data could be obtained and the mission would completely fail.

In fact, the optical system has already been introduced since it is mainly composed by the lenses. Nevertheless, the equations that govern it and the variables on which it depends have not been studied yet. It can also contain mirrors, however, for this project, this option has not been considered necessary [52] [1]. As it can be appreciated in Figure 4.13, it is expected that the optics are formed by at least three lenses, although they could be even four.

With respect to the detector, there are two main options, treated in depth in [57], to incorporate a photodetector or a bolometer. Their working processes present several differences. Photodetectors are sensors of EMR which convert photons into current, while bolometers measures the EMR by the heating of a material with a temperature-dependent electrical capacity or resistance. The characteristics of both types of detectors are presented in Chapter 6.

Despite the discussion between the two types continues to exist, one main output can be distinguished, the detector will consist on 2D pixel array (n rows x m columns).

[1] This PhD fully covers the optics design in MWIR.

5.2 Model

To study the electromagnetic radiation received by the detector, it is possible to divide the Earth in pieces. These portions are defined by the Field of View (FOV), which is the angular aperture of the payload beam. However, it is more interesting to know the FOV of a single pixel of the detector, this simplifies the calculations, called Instantaneous Field of View (iFOV). The iFOV determines the Ground iFOV, whose square root is the well known GSD, which is, neglecting the curvature of the Earth [2], the 1D portion of the Earth perceived by one pixel. The GSD is wanted to be the lower possible since it implies better imaging resolution. The sum of all Ground Sampling Distances composes the swath.

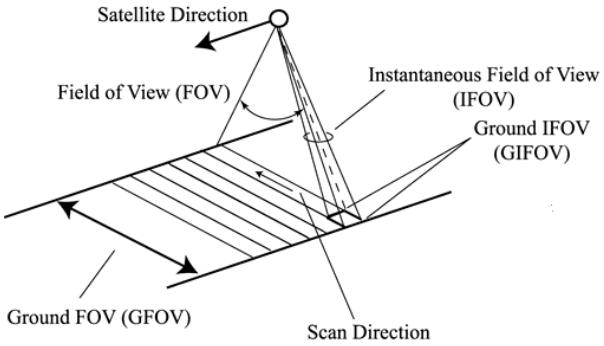

Figure 5.1: FOV and iFOV definition.

Gathering this theory with the optic system depicted in Figure 4.13, it results in:

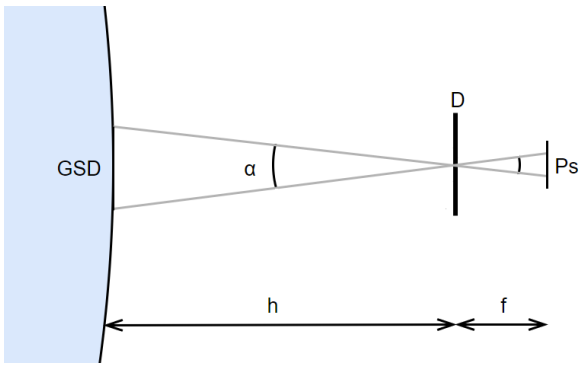

Figure 5.2: One lens model.

This model is called one lens optics and it allows to establish a relation between the main parameters that appear in the problem

$$\tan\alpha = \frac{Ps}{f} = \frac{GSD}{h} \tag{5.1}$$

Where Ps is the pixel size, f the focal length and h the height of the satellite.

Moreover, the design is controlled by the diffraction limit of the optical system in order to avoid aberration. Diffraction is the principal limit to resolution of any optical system.

[2] A study of the influence of a curved surface in GSD can be found in [18].

It results from the interaction of electromagnetic radiation with the sharp limiting edge or aperture of the optical system [53]. The diffraction limit can be determined from Airy disk [58]:

$$D_t = 2.44 \cdot \lambda f_{/\#} \tag{5.2}$$

Where D_t is going to be the minimum size of the pixel required to collect properly the signal and $f_{/\#}$ is the f-number, which can be defined, if D is the diameter of the lens (payload aperture), as:

$$f_{/\#} = \frac{f}{D} \tag{5.3}$$

5.3 Parametric study

The earlier equations define a system of three equations with six unknowns, as h is fixed by the orbit ($700km$). However, two parameters present an upper limit, the diameter and the focal length, as they must accomplish the dimensional requirements of the spacecraft. Therefore, the diameter should be lower than $0.1m$ while the focal length should be lower than $0.15m$, which is the maximum size destined to the payload.

For the first calculations, the wavelength has been fixed at 5 μm as it will be defined as the maximum wavelength of the bandwidth of study since it is the one that produces more diffraction. Therefore, the wavelength is a parameter constrained to several definite values. By performing this, the f-number only depends on the pixel size, varying linearly with it (Figure 5.3).

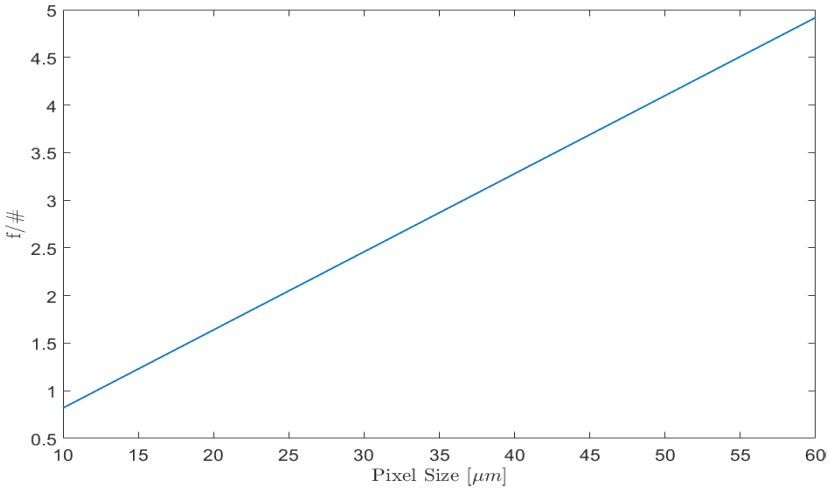

Figure 5.3: f-number vs pixel size at 5 μm.

The value obtained for the f-number is the maximum value required in order to not suffer aberrations for diffraction. An important point about the f-number is that it must be as low as possible to not have aberrations. So, looking at its formula, Equation 5.3, the diameter should be as great as possible while the focal length ought to be small. However, for a f-number

value lower than 1.5 the optic design starts to complicate considerably and for a value of 1 or lower, it becomes almost impossible.

Moreover, since the two parameters through which the design can be modified are the focal length and the diameter of the lens, the influence of these variables must be measured. Firstly, it is studied the influence of the diameter in the GSD and the focal length, as a function of the pixel size.

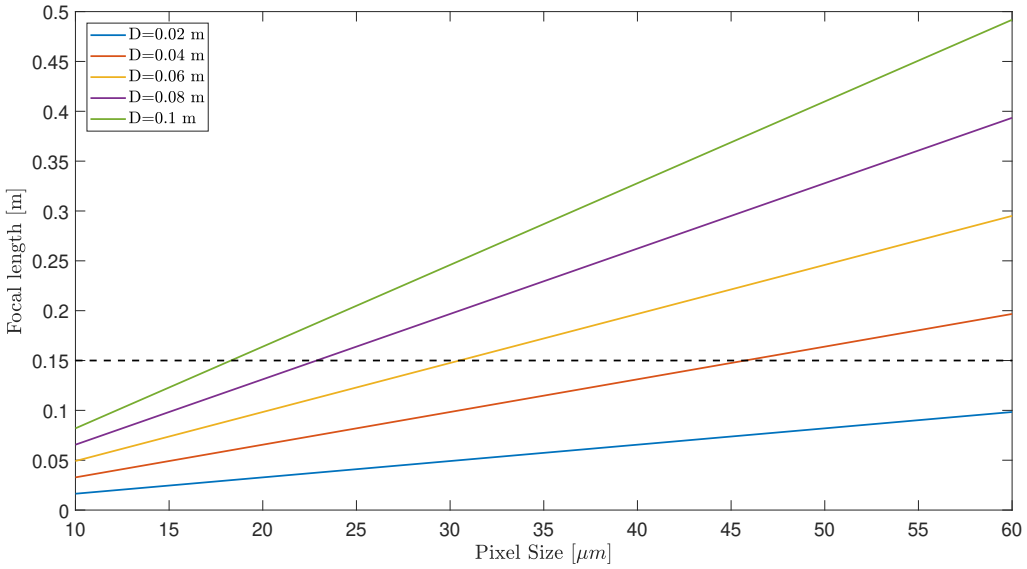

Figure 5.4: focal length vs pixel size at 5 μm for different diameters.

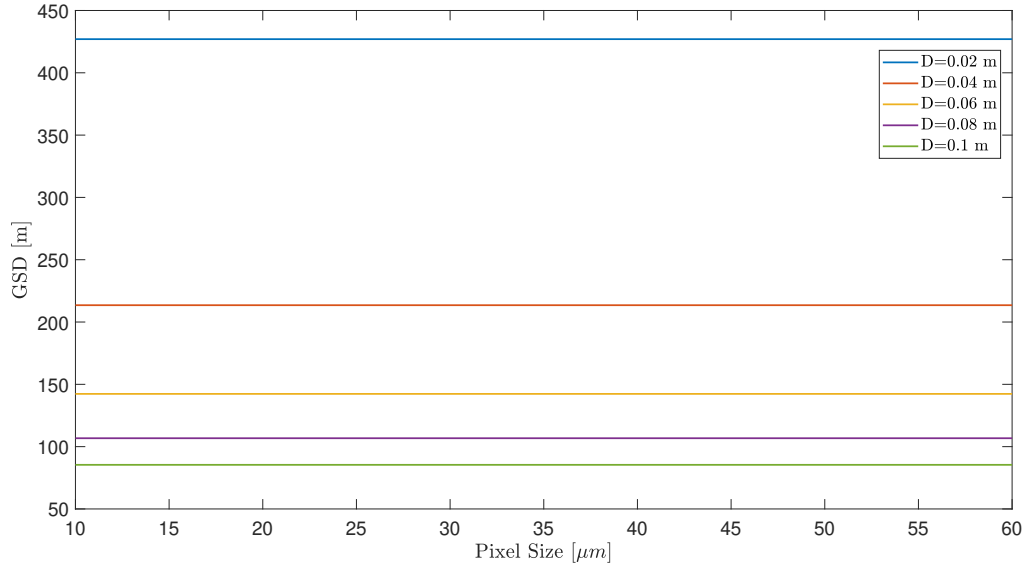

Figure 5.5: GSD vs pixel size at 5 μm for different diameters.

From Figure 5.4 one can observe the direct proportionality of the focal length with respect to the diameter. Hence, the bigger the diameter, the lower the range of pixel size available to fulfill with the diffraction and dimensional requirements. Looking at Figure 5.5 it is demonstrated that the bigger the diameter, the better resolution is achieved.

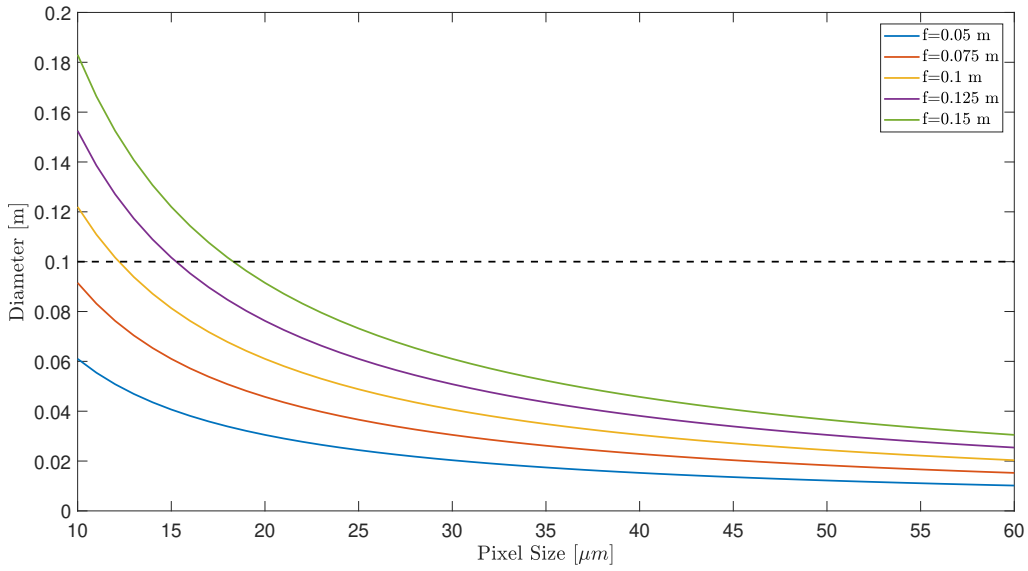

Figure 5.6: diameter vs pixel size at 5 μm for different focal lengths.

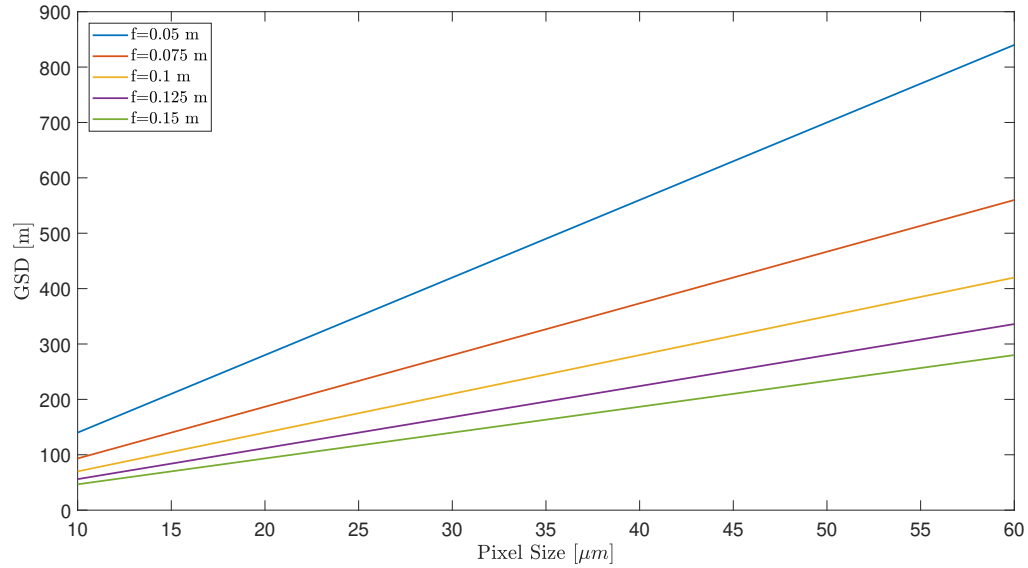

Figure 5.7: GSD vs pixel size at 5 μm for different focal lengths.

As one can appreciate in Figure 5.6, the greater the focal length, the bigger the pixel necessary to accomplish the dimensional and diffractive needs. Furthermore, in Figure 5.7 it is possible to observe how by increasing the focal length a lower GSD and a better ground resolution is reached.

Summarizing, to obtain the lower GSD possible it would be desired to have a big focal length and diameter. However, the room is limited due to the dimensions of the satellite.

Now, a comparison between the bands studied can be performed. There are three of them. For MWIR, as it was demonstrated in the comparison of the fluxes, it is not possible to obtain measures of the ground for a wavelength lower than 3.6 μm since the albedo blocks the observation. Therefore, the bands considered for MWIR will be the ones defined in

Section 4.5, one between 3.6 and 4.2 μm (MWIR-1) and another one from 4.4 to 5 μm (MWIR-2). Most detectors in MWIR work between these two ranges. On the other hand, in LWIR, the studied range includes from 8 to 12 μm, since, as it was deduced from the absorption coefficient of the lenses, it is difficult to have a good transmittance of the optic system beyond that value. To carry out this comparison, another different parameter must be fixed, in this case, the focal length has been chosen randomly, with a value $f = 0.14m$ (it is unlikely to be able to employ the whole payload length).

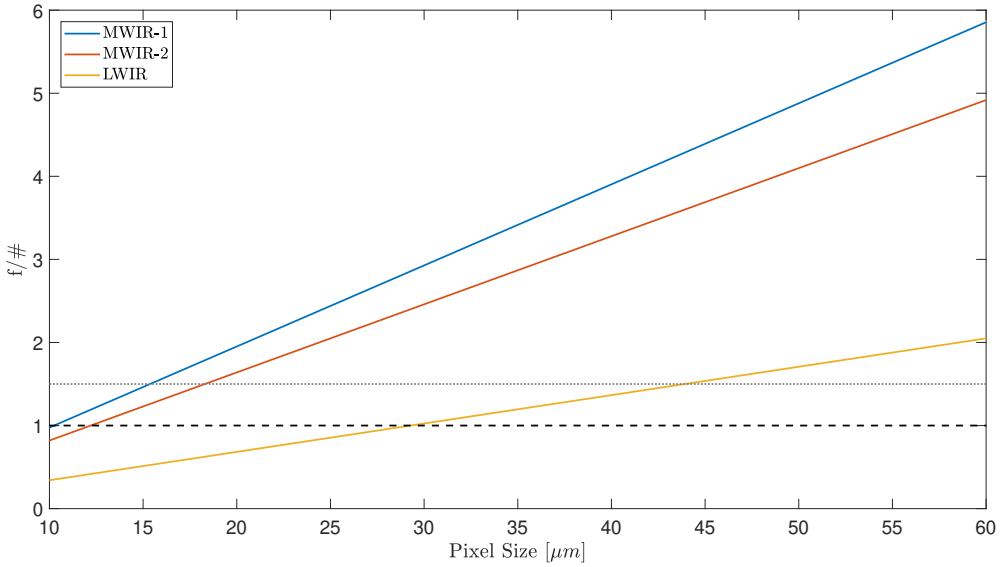

Figure 5.8: f-number vs pixel size when $f = 0.14m$ for different bands.

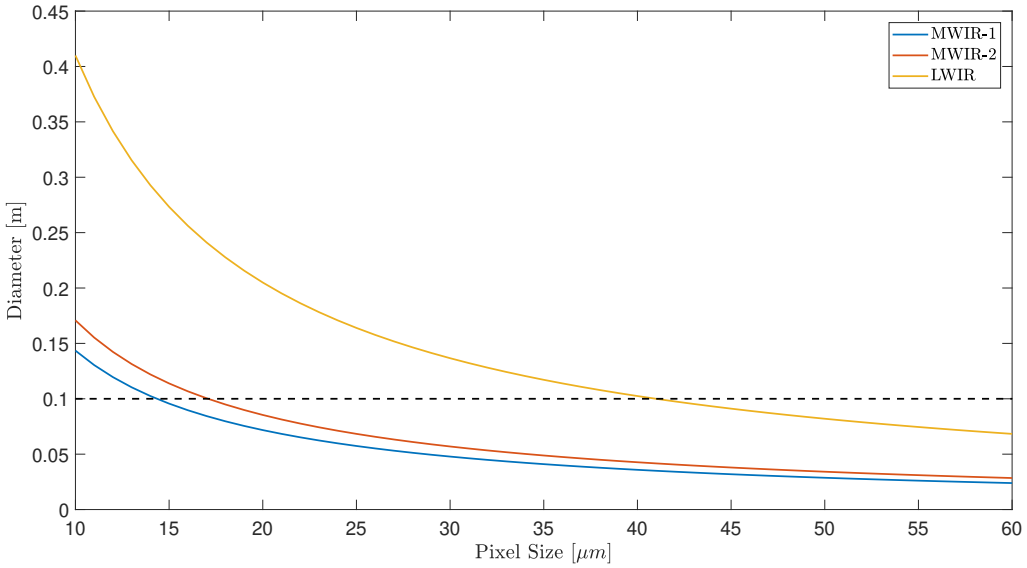

Figure 5.9: diameter vs pixel size when $f = 0.14m$ for different bands.

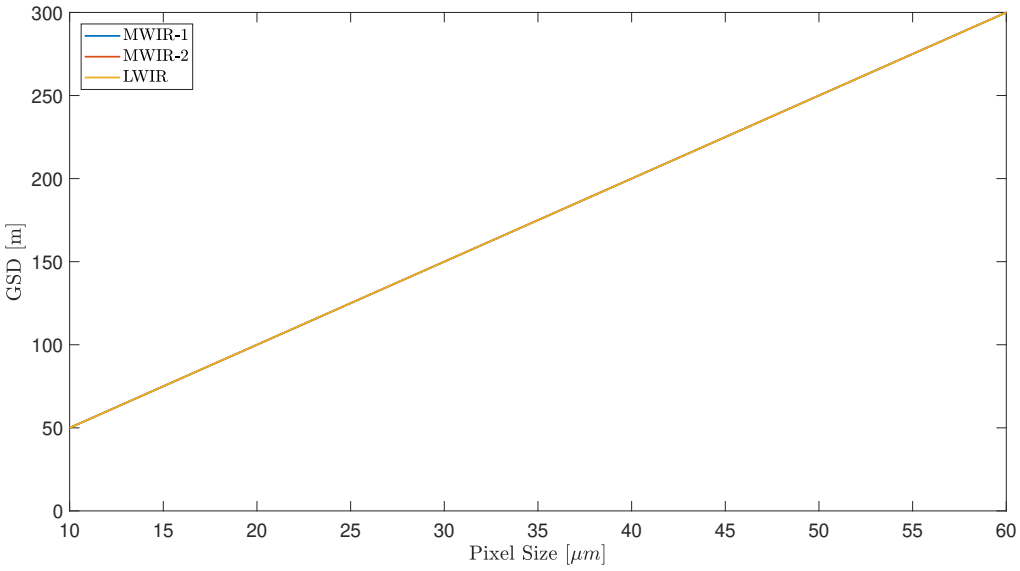

Figure 5.10: GSD vs pixel size when $f = 0.14m$ for different bands.

The main conclusion reached from these graphs is that as the wavelength increases, the pixel size required to avoid diffraction rises, reducing the spatial resolution. For instance, in MWIR-1, with a pixel size of 20 μm, one can obtain a $f_{\#}$ close to 2, satisfying the dimensional requirements and with a GSD around 100 m. On the other hand, in the LWIR band, it would be needed a pixel size around 45 μm to have an acceptable f-number that adjusts to the dimensional needs, obtaining a GSD around 230 m. Therefore, for LWIR the spatial resolution is deteriorated more than the double compared with MWIR.

Commercial detector's pixel size is usually between 15 and 30 μm. So, to obtain a pixel size of 50 μm as it might be required in LWIR it is usually employed a technique known as binning. Through binning, two or more pixels are combined into one large pixel whose size it is the sum of the small ones. This method is applied sometimes in order to rise the SNR and shorten the read out time, despite losing resolution. In this case, it must be used to increase the pixel size and achieve the needed f-number. Based on the parametric study, with a binning factor of 4 (2x2), where each two pixel are combined, it should be enough.

6 | Signal to Noise Ratio

The Signal to Noise Ratio (SNR) is one of the main parameters to calculate in order to know if the mission will be successful. It is the ratio between the signal captured by the detector from the scientific source, crops in this project, with respect to the noise produced during the measures. It characterizes the quality of the measurement.

In this chapter the SNR in OUFTI-Next's mission will be studied. To perform it, it is firstly necessary to define the sampling times that appear in the issue. After that, the signal arriving to the detector will be calculated. Next, the noise will be computed, introducing the NETD and detectivity. Finally, a parametric study of the SNR is carried out to evaluate how the different variables affect this parameter.

6.1 Times

Several times of great importance intervene in the problem. The satellite is travelling through the space, perceiving different portions of the Earth at a time. Furthermore, the detector counts with a response time to detect the photons. Moreover, the pixels takes a precise time collect photons, up to its saturation time which implies maximum photon capture. Finally, the electronic system takes some time to read out the photons and convert them in electrical current.

The first sampling time analysed is the time that the satellite takes to travel the GSD. This time depends on the orbital velocity of the spacecraft and the dimension of the GSD.

Knowing the altitude of the orbit ($h = 700\ km$) it is possible to compute its orbital velocity. Assuming the SSO is circular, the orbital period is:

$$T_o = 2\pi\sqrt{\frac{r^3}{\mu_e}} \tag{6.1}$$

Where $\mu_e = 398600.4418\ km^3/s^2$ is the gravitational parameter for the Earth and r is the radius of the orbit. Once the period is computed, the orbital velocity with respect to the ground can be computed as:

$$V_{sat} = \frac{2\pi}{T_o} r - \omega_{earth} \cdot R_{earth} \tag{6.2}$$

Where $\omega_{earth} = 7.2921159 \times 10^{-5}\ rad/s$ is the Earth angular velocity. Eventually, the exposure time is calculated as

$$t_{i,sat} = \frac{GSD}{V_{sat}} \tag{6.3}$$

Hence, $t_{i,sat}$ is the integration time of the satellite, this is the time that the spacecraft sees a GSD before passing to the next one. The detector has to be able to collect the photons and read them out before this time. Otherwise, the images is blurred as the detector is still integrating a GSD when the next one is perceived.

Next, the frame rate is considered, it is a function own of each detector and is measured in Hz or FPS (frames per second). It is the sum of the exposure time, t_e and the read-out time, t_{ro}. The exposure time is the time that the pixel is collecting photons. It is maximum if the pixel reaches saturation, although it does not have necessarily to be this value. Furthermore, during the exposure, the integration of the signal by the circuit is carried out, converting photons into electrons. The integration time of the circuit uses to be estimated as half of the frame rate of the detector, and so will be calculated in next computations. Despite in reality integration time of the circuit is a little greater than exposure time, both are considered to be equal. Moreover, the read-out time is the time that takes the charge passed from the pixel to be converted into voltage. Eventually, the electronic signal goes to an electronic device to obtain an image and a new frame starts. As it has just been mentioned, the sum of the integration time of the circuit and the read-out time must be shorter than the integration time of the satellite to finish the image taking before the pixel passes to see the next GSD.

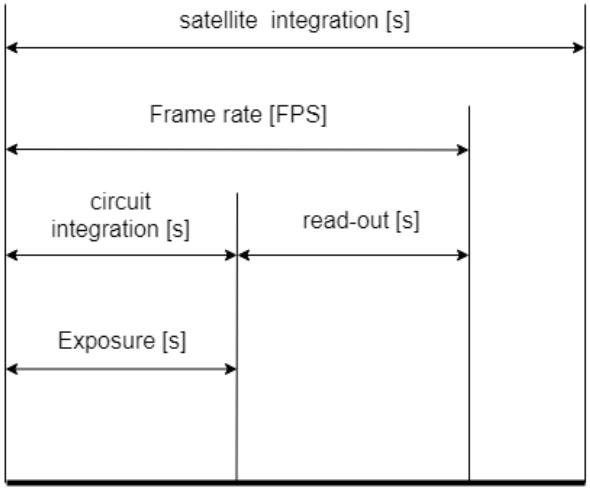

Figure 6.1: Sampling times.

Finally, there is one more time that needs to be addressed, the response time, t_r, which is the time that takes the detector to start to capture photons once the signal arrives, it is specially important in bolometers and it can affect the whole observation, reason why it will be fully studied in Chapter 7.

6.2 Signal

The total signal can be computed from the sum of the radiant flux or radiant power of each component. However, the detector does not differentiate where this signal comes from, it only counts the total number of photons. Therefore, one must look for a waveband where the vast majority of the signal is due to the ground emittance, as the rest of sources will perturb this one. Otherwise, one would need a very complex model which, from the number of photons detected, discounts the contribution from undesired sources and obtain the flux coming from the ground.

Therefore, it is important to estimate the radiant power of each component of the radiometric budget. To do so, it is usually calculated the radiant power that reach each pixel of the detector. If one wants to know the total power that the detector perceives, it would only be necessary to multiply the radiant power on one pixel per the total number of pixels that compose the detector, assuming that the source is homogeneous.

6.2.1 Radiant power in one pixel

If one looks at the units of the spectral radiance $\left[\frac{W}{sr \cdot m^2 \cdot \mu m}\right]$, it is possible to realize that in order to convert the spectral radiance into radiant flux [W], it is necessary to integrate for the wavelengths considered and to multiply per the view angle of the source with respect to the payload aperture and the source surface. However, since these parameters are difficult to compute, it is possible to use the etendue or throughput to use easy-measured variables. The etendue is the product of the cross-sectional area of a beam and its projected solid angle and that accomplish the following: it is invariant for a case in which the source image fills the detector [30].

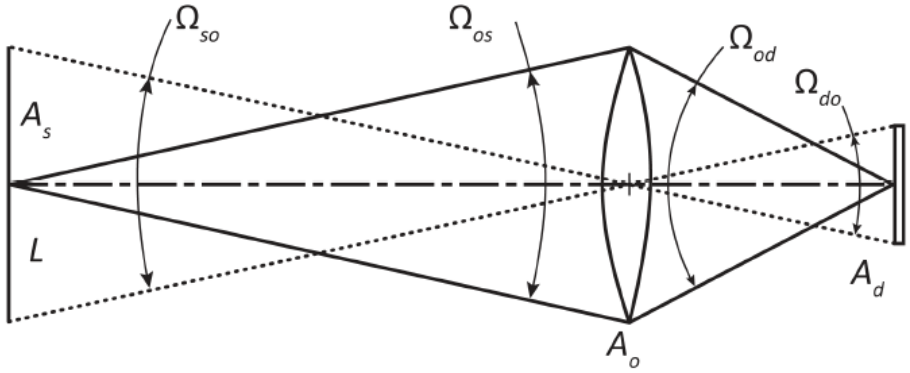

Figure 6.2: Invariance of throughput for a case where the source image fills the detector.

$$A_s\Omega_{os} = A_o\Omega_{so} = A_o\Omega_{do} = A_d\Omega_{od} \tag{6.4}$$

Where A_s is the area of the source, A_o is the area of the optics and A_d is the area of the detector $A_d = (m \times n)ff \cdot Ps^2$, being m and n the number of rows and columns, respectively, and ff the fill factor of the pixel, which describes the ratio of light sensitive area versus total area of a pixel. This ratio is less than 1 since a part of the area of a pixel is always used for transistors, electrodes or registers, which belong to the structure of the corresponding image

sensor. Whereas, Ω_{pq} represents the solid angle that p subtends at q. Of course, to carry out the calculation for one pixel, A_d must be divided by the number of pixels, so for what it continues, $A_d = ff \cdot Ps^2$. Normally the two parameters used to compute the etendue are the detective area of the pixel and the solid angle of the optics, which is related with the optical design.

$$\Omega_{od} = \frac{\pi}{4 f_{/\#}{}^2} \; [sr] \tag{6.5}$$

And so, the radiant flux of the component "i" can be calculated as:

$$P_i = \int_{\lambda_{min}}^{\lambda_{max}} L_i A_d \Omega_{od} \tau_{opt} \; d\lambda \; [W] \tag{6.6}$$

Where τ_{opt} is the transmissivity of the optics. As the material of the lenses is not defined yet, it is not possible to establish its dependency with the wavelength and so, a conservative value of 0.9 (based on Table 4.3) is selected for the future numerical calculations.

It may be also useful to compute the number of photons per unit of time that reach one pixel. It is more frequent to work with photons when the power is very low like in this case. To obtain it, one needs to divide the power by the energy of a photon, therefore.

$$F_i = \int_{\lambda_{min}}^{\lambda_{max}} L_i A_d \Omega_{od} \tau_{opt} \; \frac{\lambda}{h\,c} \; d\lambda \; \left[\frac{photon}{s}\right] \tag{6.7}$$

Now, it is possible to convert the flux of photons into number of electrons per second multiplying per the quantum efficiency of the detector, which is its capability to convert photons into electrons.

$$Fe_i = F_i \; \eta \; \left[\frac{e-}{s}\right] \tag{6.8}$$

If one desires to compute the total number of photons or electrons that arrive to the pixel to take one image it is necessary to multiply the flux of photons or electrons per the exposure time, t_e. Therefore, the bigger the exposure time, the greater the signal received, until a value of t_e when the pixel reaches its maximum capacity to collect photons, called saturation time.

In order to know which might be the most interesting band for the observation among the three proposed, a study of the radiant power of each component, in term of flux of electrons, has been performed. For the payload component, only the worst case has been considered, when the payload is at the highest temperature expected (260 K).

It can be observed in Figure 6.3 how in MWIR-1 band (3.6-4.2 μm) to overcome the albedo the temperature in ground must be above 282 K, which is an event that do not always happen. Furthermore, whereas the payload component is very low compared with the other two, the albedo has the same order of magnitude than the ground emittance component, affecting negatively the observation as it disturbs the scientific signal.

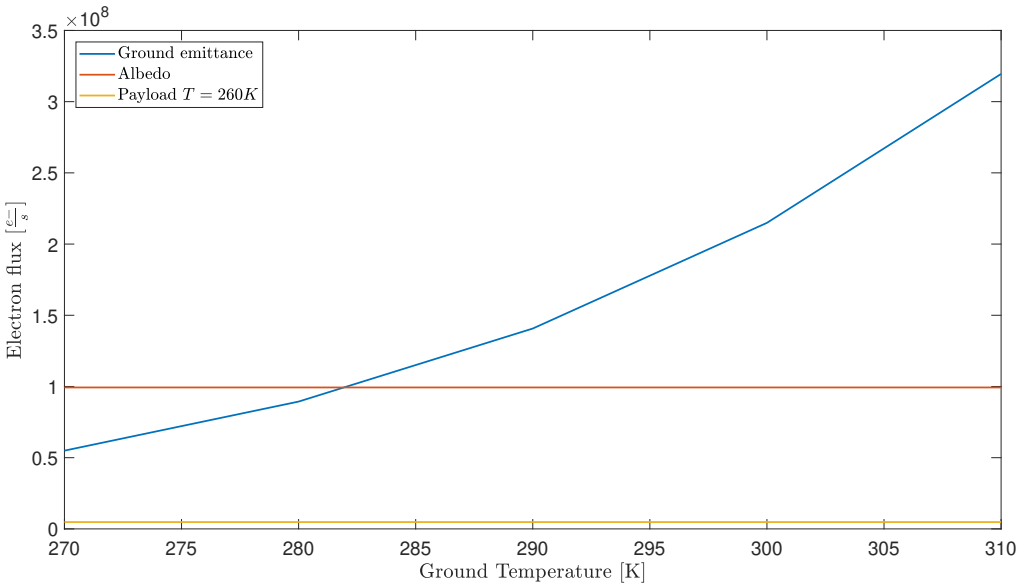

Figure 6.3: Number of electrons from the different components in the band MWIR-1. Values obtained for: $GSD = 100\ m; Ps = 15\ \mu m; f = 0.105\ m; D = 0.072\ m; f_{/\#} = 1.46$

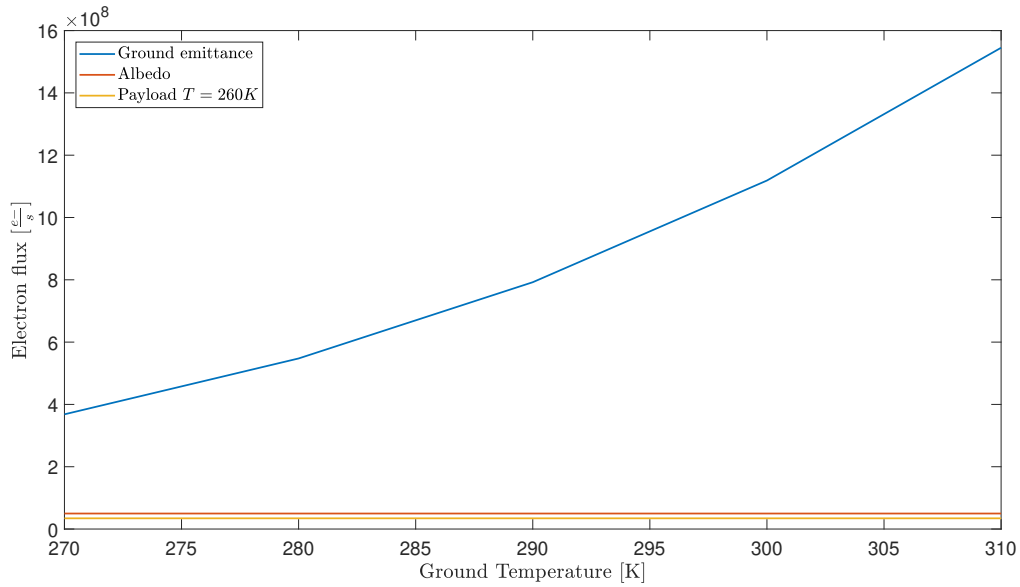

Figure 6.4: Number of electrons from the different components in the band MWIR-2. Values obtained for: $GSD = 110\ m; Ps = 18\ \mu m; f = 0.115\ m; D = 0.078\ m; f_{/\#} = 1.48$

Figure 6.4 shows the electron number perceived from each component for MWIR-2 band (4.4-5 μm). One may appreciate this band is better for observation in MWIR than MWIR-1 as ground component is much bigger than the other two, producing a clearer signal. Reason why this band will be the one analysed for the SNR in MWIR.

Finally, in Figure 6.5, it is possible to note that this band collects the largest quantity of electrons coming from the ground emittance component therefore, it is the band with the highest sensitivity. Moreover, albedo component is lower than payload component, but both of them are negligible compared with ground's radiation.

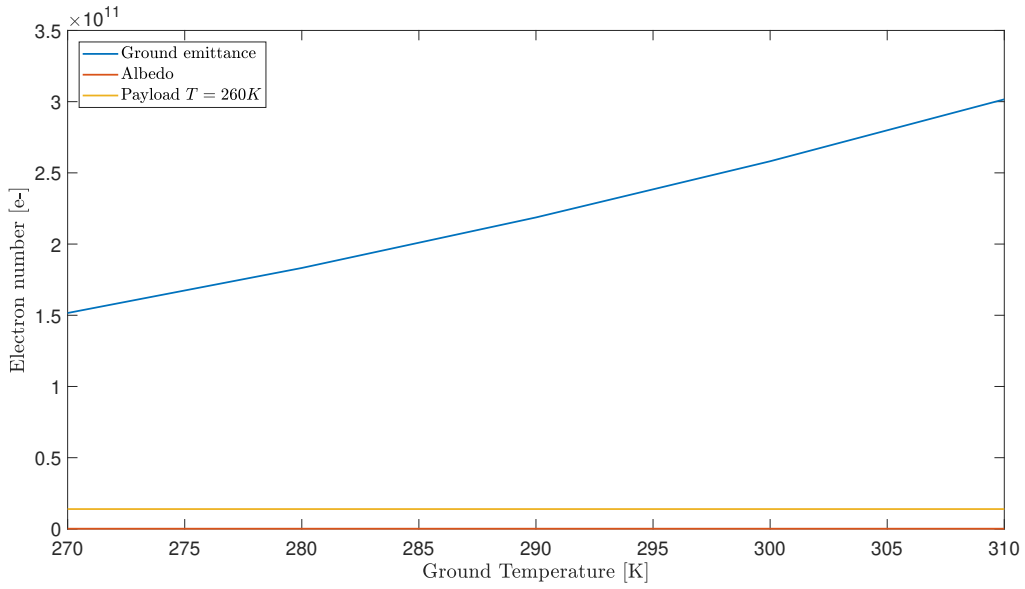

Figure 6.5: Number of electrons from the different components in the band LWIR. Values obtained for: $GSD = 235\ m; Ps = 25\ \mu m\ (binning\ factor = 4); f = 0.149\ m; D = 0.087\ m; f_{/\#} = 1.71$

6.3 Noise

The noise consists of the undesirable signal components arising in the electronic system. It depends on both, the detector and random fluctuations of the arriving signal and as the magnitude of noise increases, uncertainty in the measured signal becomes greater. It must be outlined that the study of the noise on the detector was performed in collaboration with [57], master's thesis in which one can find a more detailed study of the sources of noise and how much it is influenced by the detector type.

6.3.1 Sources of noise

In IR imagers there are several noise sources, which depends on the type of detector employed. The two types of detectors considered for the research have already been introduced, but it is necessary to go further with their characteristics. Their methods to operate are very distinct. While photodetectors are based on semi-conductor technology to convert photons collected into electrons, bolometers measure incident electromagnetic radiation via the heating of a thin metal layer with a temperature-dependent electrical resistance and need to be isolated from external heat sources.

Photonic detector, photon detectors or simply photodetectors are usually based on indium antimonide (InSb) or mercury cadmium telluride (HgCdTe). They present very fast response speeds and high sensitivity. However, they need to operate at low temperature, requiring an active cooling system to perform, which implies more room occupied, more power needed from the solar panels and more weight [59]. Besides, they have low quantum efficiency and are expensive.

On the other hand, bolometers are composed in general by vanadium oxide (VOx), although amorphous silicon (a-Si) is also common [59]. Their main advantage is the fact that they are able to operate at room temperature so, no need of cooling system. However, they present more noise, less sensitivity and specially, a very slow response due to their operation method. A derivative of bolometers are microbolometers which are essentially the same but in a micro scale, more interesting for this project. They basically operate in LWIR although new technologies have been developed also for MWIR.

The first noise is photon noise or shot noise, it results from the inherent statistical variation in the arrival rate of photons incident on the detector. It is associated with the non-equilibrium conditions in a potential energy barrier of a photovoltaic detector through which a dc current flows [60]. It highly affects photodetectors whereas bolometers are not influenced by it.

$$i_S^2 = 2Q_e^2\eta\phi_{ph,sig}f + 2Q_e^2\eta\phi_{ph,bkg}f \tag{6.9}$$

Where $Q_e = 1.6022 \times 10^{-19}C$ is the electron elementary charge, $\phi_{ph,sig}$ is the photon flux of the signal and $\phi_{ph,bkg}$ is the photon flux of the background or undesired signal (albedo and payload components).

Next, dark noise, it arises from a statistical variation in the number of electrons thermally generated in the detector [30].

$$i_{DC}^2 = 4Q_e i_0 f \tag{6.10}$$

Where i_0 is the dark current which highly depends on detector's temperature:

$$i_0 = C_r \cdot A_d \cdot T_d^2 e^{(-\frac{E}{k \cdot Td})} \tag{6.11}$$

Where $C_r = 1.20173 \times 10^6 \frac{A}{m^2K^2}$ is Richardson's constant, T_d detector's temperature and E the bandgap energy, a property of the material used.

Next, the thermal or Johnson noise is due to fluctuations in velocity. It exists even without electric bias. It is a consequence of stochastic motion of electrons within a material with finite resistance and it shows a way to keep thermal equilibrium in a semiconductor [61].

$$i_J^2 = 4\frac{kT}{R}f \tag{6.12}$$

Being R the resistance of the semiconductor material.

Moreover, I/f or flicker noise is a consequence of stochastic fluctuations of either the density of free carriers or their mobility [61]. It is always present in microbolometers and photoconductors, because there is always a dc-bias current flowing within the detector material. Alongside with Johnson noise, flicker noise is the main noise that affect uncooled bolometers, while photodetectors are few perturbed by both of them.

$$i_F^2 = \kappa \frac{i^{\alpha_{1/f}} f}{f^{\beta_{1/f}}} \tag{6.13}$$

Where κ is the proportionality factor or I/f parameter, i the current through the detector, f the frequency corresponding to the bandwidth studied and $\alpha_{1/f}$ and $\beta_{1/f}$ are numerical constants whose typical values are 2 and 1, respectively.

Now, to convert these currents or charge fluxes ([A=C/s]), into electrons, it is necessary to divide them by the electron charge and multiply per the integration time of the electric circuit, $t_{i,elec}$.

$$N_i = i_i \frac{t_e}{Q_e} \tag{6.14}$$

Preamplifier noise N_{PA}, which has to do with readout noise, might also be important. Preamplifiers are used to amplify weak signal and provide better conditions for the operation. However, a perfect measure of the charge in the clump of electrons cannot be performed. Usually, the right value on average is yielded, but with some random scatter, which is taken into account by this noise. The preamplifier noise use to be given by the manufacturer as a number of electrons per pixel.

These are the main noises considered although there are some more such as temperature noise for bolomoters or generation-recombination noise for photodetectors.

So, one can compute the total number of electrons due to the noise as:

$$N = \sqrt{N_S^2 + N_{DC}^2 + N_J^2 + N_F^2 + N_{PA}^2} \tag{6.15}$$

6.4 SNR

The SNR is the rate between the measured signal and the noise. A large signal-to-noise ratio is important in the acquisition of good quality images.

6.4.1 Calculation

It is feasible to compute SNR through the calculation of the radiant flux of the signal divided by the direct computation of the noise, both of them in the same units. However, Equation 6.15 shows a complex method to perform it since noises present on this equation depends on very particular parameters which are not often provided by manufactures. Therefore, it is necessary to find a simpler way to calculate SNR with the suitable variables [60].

$$SNR = P \cdot DET \tag{6.16}$$

Equation 6.16 calculates SNR in function of two variables, P, the incoming radiant power [W] that can be computed from Section 6.2 considering only ground component and DET,

which is the detectivity of the detector in [W^{-1}]. The detectivity describes the performance of the detector, as it is a measure of its ability to detect the signal.

$$DET = \frac{4f_{/\#}^2}{Ad \cdot \pi \cdot \zeta \cdot NETD \cdot (dL/dT)_{target}} \tag{6.17}$$

Where $(dL/dT)_{target}$ is the derivative of the radiance of the target (ground component) with respect to the temperature, $\zeta = 0.9$ is a coefficient to take account of a filter collocated before the optics [57], and NETD the Noise Equivalent Temperature Difference, which is the only unknown parameter in the equation. The NETD determines the temperature resolution achieved in the mission as it is defined as the minimum temperature change of the target that can be detected by the optical instrument. Therefore, it is the minimum temperature change that produces an output signal in the detector of the same value as its total current noise. It is a value that depends on the detector and wavelength, is lower for photodetectors and MWIR.

NETD value is usually given by detector's sellers, measured for a $f_{/\#}$ equal to 1 and a $(dL/dT)_{target}$ of a black body at a certain temperature measured in ground so that, transmissivity and emissivity are not considered as it must be done for the NETD obtained from space. Therefore, NETD given by manufacturers is not the same one obtained in space, in contrast to detectivity that can be considered as constant for a given detector.

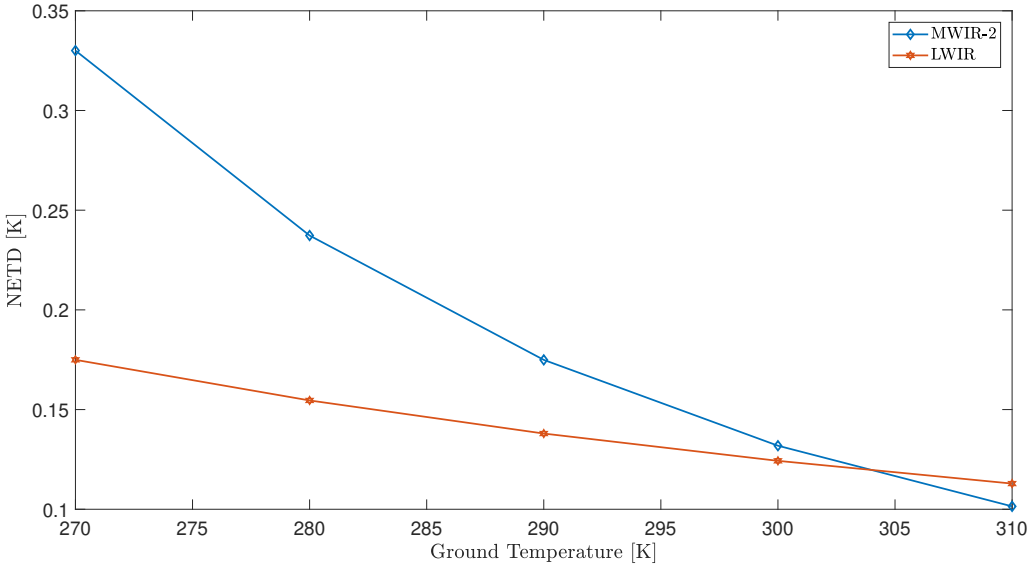

Figure 6.6: NETD in space vs ground temperature for MWIR-2 and LWIR.

It is complicated to establish a comparison of the NETD obtained in the space in function of the waveband since it is not a direct function of wavelength. However, in Figure 6.6 a result has been performed, defining the parameters on which NETD depends based on typical values for the corresponding waveband. For MWIR $f_{/\#} = 1.5$ and $NETD = 23\ mK$ while for LWIR $f_{/\#} = 1.5$ and $NETD = 44\ mK$. One can appreciate that the NETD achieved in the space in LWIR is lower and more stable with the variation of the temperature in ground, which is desired. However, as the temperature of the ground increases, NETD in MWIR tends to reduce and at some point, around 305 K in this example, NETD is lower for MWIR. Furthermore, it must be outlined that for both bands, the values obtained for this parameter are expected to be good enough to perform the observation.

6.4.2 Parametric study

Finally, a study of the variation of the SNR with different parameters is carried out. Firstly, in Figure 6.7 it is showed how SNR change in function of the ground temperature, increasing with it. This is something expected as the greater the ground temperature, the larger the signal received and so, SNR rises. It is also possible to observe that when the NETD provided by the manufacturer decreases, the SNR rises as the detectivity is greater.

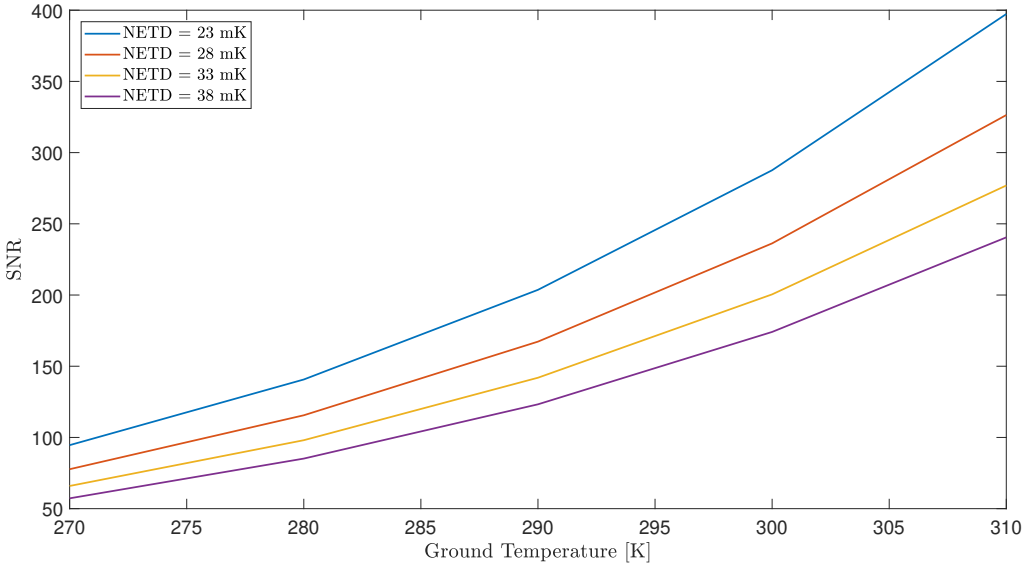

Figure 6.7: SNR vs ground temperature for different NETD.

Next, in Figure 6.8 it is possible to see that the effect of a rise in f-number means a decrease in the SNR.

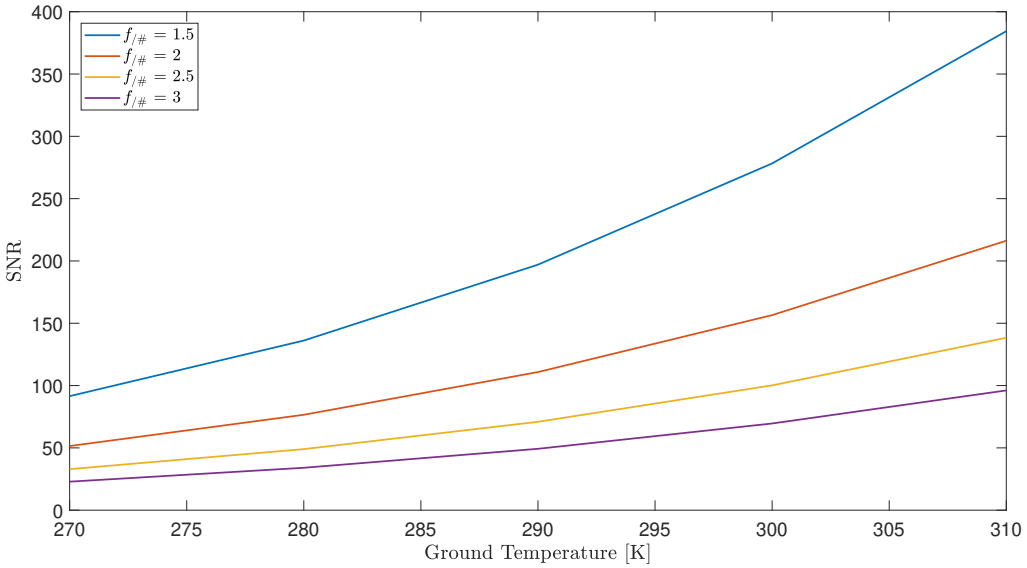

Figure 6.8: SNR vs ground temperature for different f-number.

Lastly, when comparing the SNR for different wavelengths one may find an issue, the SNR does not depend directly on this parameter as it occurs with the NETD in the space, but in others which are obtained from it such as the different values of the optics. However, based on the results yielded in Section 6.2.1, where it was observed how in LWIR the signal received is two orders of magnitude greater than in MWIR, it is feasible to expect that SNR in LWIR is better than in MWIR.

7 Signal treatment

The detector counts an number of photons per unit of time, this is the signal received. It varies with time as the satellite moves through space, producing that each pixel sees a new GSD, with a different radiant power. The measured signal must be worked in order to obtain the desired output, the ground temperature.

This chapter studies briefly the analysis of the signal once it arrives to the detector and the importance of the response time in the measurements in MWIR and LWIR. While the previous chapters were more focus only in the differences between the two bands studied, this one also reports the comparison between the two type of detectors around the topic of the response time.

7.1 Conversion

The detector collects photons, converts them into electrons and those to electric current so that an image is obtained. Knowing the equations involve in the problem it is possible to finally compute the temperature of the ground, which is the goal of this project. An ideal conversion of the input signal, assuming, once again, that the only signal perceived is from the ground, could be as shown in Figure 7.1.

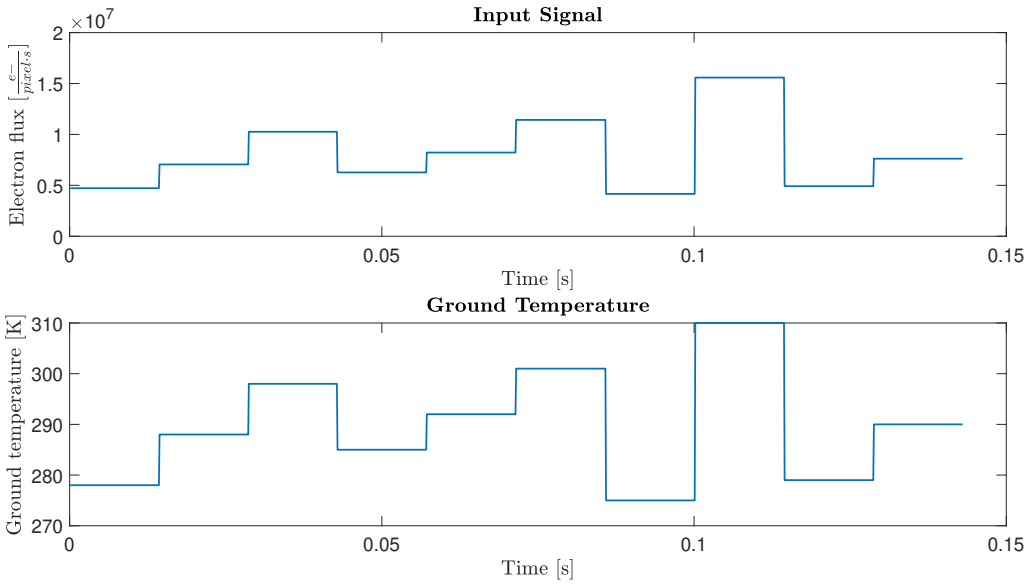

Figure 7.1: Ideal signal conversion.

In the earlier figure it is possible to observe the ground temperature yielded from a flux of electrons defined as a piecewise function where each step corresponds to the integration time of the satellite. However, there is one parameter that must be taken into account. Detectors do not change output state immediately when an input parameter variation occurs. Instead, output state will change to the new one over a period of time, called the response time. The response time can be defined as the time required for a sensor output to change from its previous state to a final settled value within a tolerance band of the correct new value. Therefore, the actual analysis of the incoming signal would be more similar to:

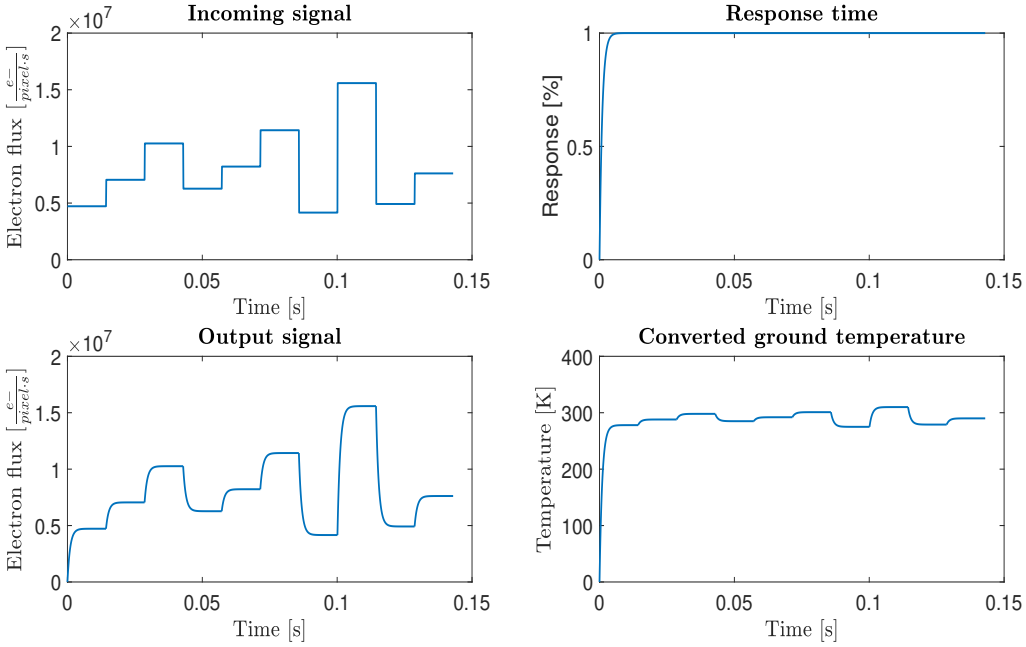

Figure 7.2: Real signal conversion for a response time of 5 *ms*.

In Figure 7.2 the delay in the signal output can be observed. The signal to analyse would be the product of the ground signal with the response time of the detector. This must be considered to obtain the right value of the ground temperature and achieve a good imaging.

7.2 Response time influence

The response time of the detector is completely different depending on its typology. Photodetectors have a response time in the order of the microseconds ($\sim$ 3-5 μs) so, the output signal can be considered as the ideal step signal. However, bolometers follow an exponential response determined by their thermal time constant, being their response time of the order of miliseconds ($\sim$ 20-50 *ms*), fact that can ruin de entire observation.

The thermal time constant is the time required for a thermistor to change 63.2% of the total difference between its initial and final body temperature when subjected to a step function change in temperature, under zero power conditions. Typically, to measure absolute temperatures 3 times the duration of the TTC (95%) is required to represent correctly the input signals. This value is measured by inducing power to the thermistor, until it heats up to a certain temperature above room temperature. After that, the power is removed and bolometer's

temperature is monitored, when it reaches a value equal to the 63.2% of the difference between the experiment temperature and room temperature, that time is considered as the TTC. It is determined by the thermal mass and thermal conductivity, but, normally, the larger the size of the thermistor, the longer the thermal response.

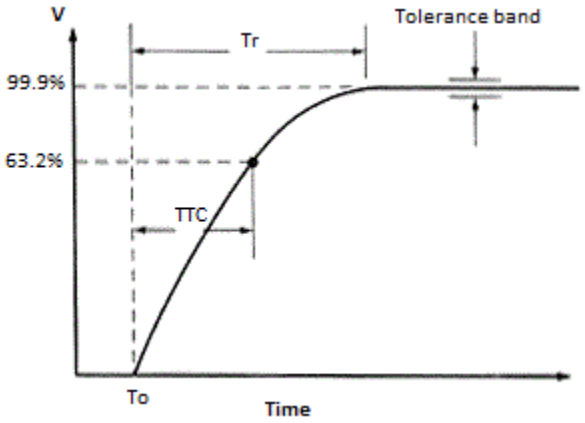

Figure 7.3: Response time.

As it was mentioned before, the sum of the integration time of the circuit and the read out time needs to be smaller than the integration time of the satellite, otherwise the images yielded would not have a good quality. Therefore, when adding the consideration of the response time, the sum of the response time plus the earlier two times must be smaller than the integration time of the satellite to achieve a suitable observation. Usually, the TTC of bolometers is between 7-16 *ms*. For this study, the integration of the signal by the electric circuit is considered to be occurring immediately as the detector perceives the input signal.

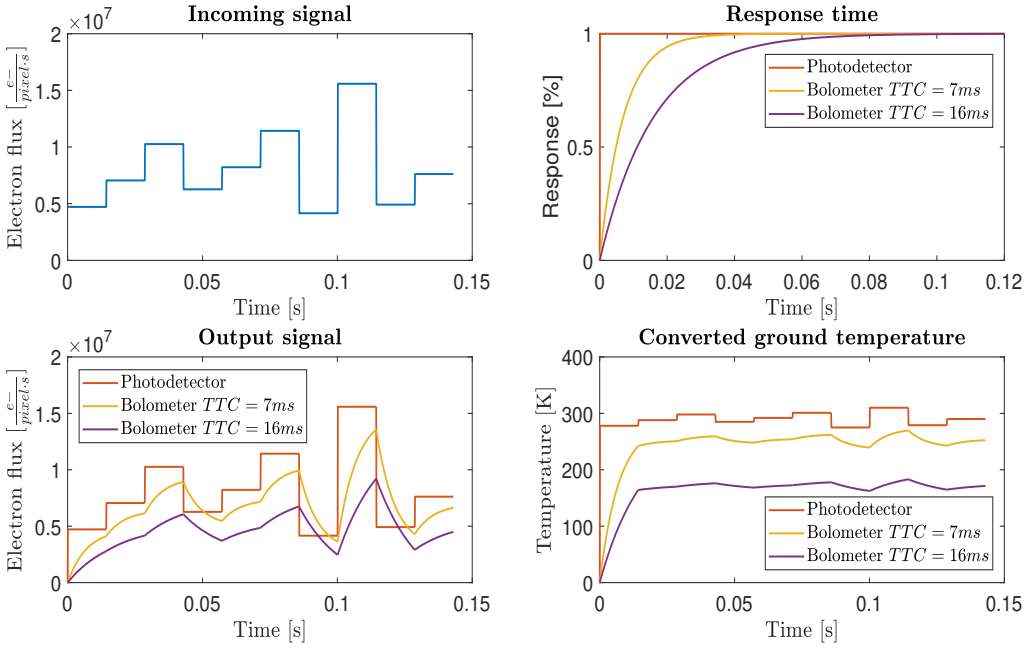

Figure 7.4: Influence of the response time in the signal analysis in MWIR.

As one can appreciate in Figure 7.4, only with a photodetector good results can be yielded

in MWIR. The photodetector represents perfectly the step function, whereas with a bolometer, even considering one with the shortest TTC achievable ($TTC = 7\ ms$), it is not possible to analyse correctly the input signal. This is due to the fact that the response time of the bolometer is bigger than the integration time of the satellite, $t_{i,sat} = 14.3\ ms$ (Result from Equation 6.3 with a GSD=100 m), which provokes that when the satellite passes to the next GSD, the bolometer has detected, in the best case considered, 87% of the input signal and only 60% in the worst ($TTC = 16\ ms$). In fact, to perform the detection of 95% of the input signal, as it is usually required for observation, one would need a bolometer with a TTC around 5 *ms*, something which cannot be found currently in the market. This means that the observation with a bolometer is not feasible in MWIR.

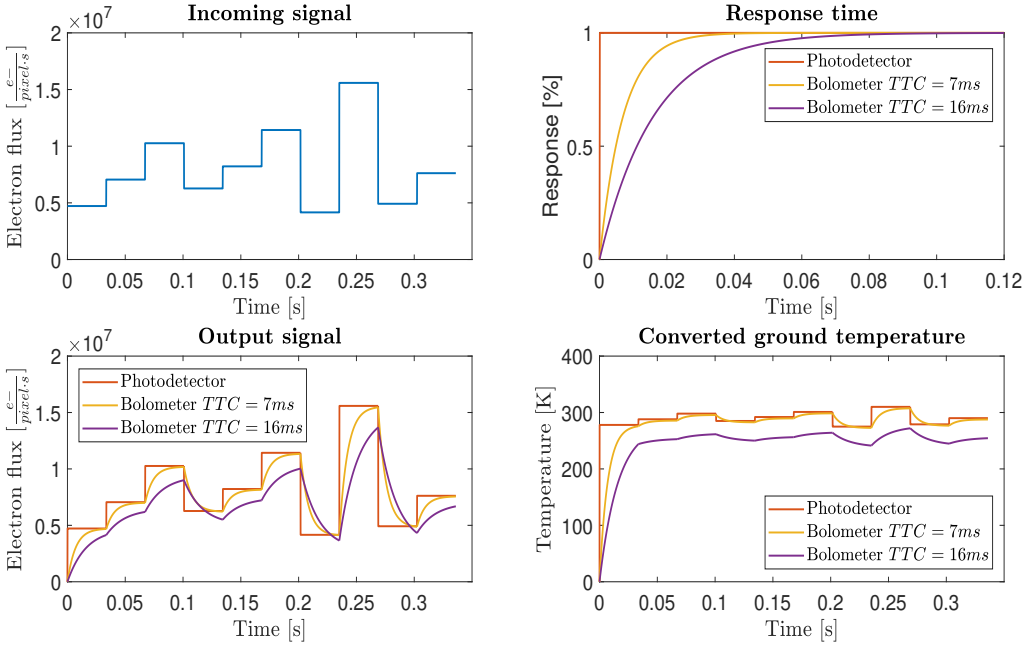

Figure 7.5: Influence of the response time in the signal analysis in LWIR.

Figure 7.5 shows a different situation for LWIR. As the integration time of the satellite is bigger, a bolometer can be a good choice. If the integration time of the satellite is $t_{i,sat} = 33.6\ ms$ (Result from Equation 6.3 with a GSD=235 m), one can appreciate how good results can be obtained with both a photodetector and a bolometer with a not very long response time. In this case with a $TTC = 7\ ms$ the 99% of the signal would be yielded. But, theoretically, using a bolometer with a $TTC = 11\ ms$ would be enough to obtain 95% of the input signal and perform the observation.

8 | Conclusions

The goal of this project was to address the possibility of converting OUFTI-Next MWIR imager into a dual band infrared CubeSat, operating in MWIR and LWIR. To do so, firstly was calculated the radiometric budget of the detector. Three fluxes were considered: albedo, ground emittance and the satellite itself. It was observed three interesting bands to perform the observation. In MWIR, the observation is not feasible for wavelengths below 3.6 μm since the majority of the radiation received is from the albedo. Two observable bands are for MWIR, for 3.6-4.2 μm and for 4.4-5 μm, separated because of atmospheric absorption. The first one, MWIR-1, is clearly affected by albedo component which could disturb the image taking while the second one, MWIR-2, is dominated by the ground emittance as the albedo and the radiation from the satellite are almost negligible. For LWIR, the observation could be carried out in the entire waveband since the ground emittance is greater than the other two components and, besides, this term is several times bigger than in MWIR. The contrast in the IR was also studied. It was observed that the contrast is higher in MWIR, which allows to differentiate better the target from the background and to appreciate some details in the image.

Secondly, the optical system of the satellite was evaluated with a parametric study for different focal lengths, diameters and wavebands. It was concluded that with the current dimensional constraints it is possible to install the optics. However, while in MWIR the GSD achieved will be around 100 m, if one desires to allocate the optics in the available space of a 3U CubeSat, for LWIR the loss of resolution is very important, doubling the value in GSD. Moreover, in LWIR it would be necessary to apply a binning to the pixels of the detector to reach the f-number required to avoid diffraction aberration.

After that, the flux of electrons for one pixel of the detector were computed for the two bands and the three sources (albedo, ground and satellite). Observing that, certainly, MWIR-1 band is considerably affected by albedo and so, MWIR-2 band would be more interesting from a radiometric point of view. Whereas the power for LWIR is two order of magnitude greater than the one perceived in MWIR, reason why the SNR is expected to be bigger in LWIR, which means a greater sensitivity. Also, the NETD and the detectivity of the detector were introduced. It is thought that the NETD obtained in the mission for any of the bands satisfies the requirements of the observation.

Finally, the effect of the response time was considered in the model. It could be observed how for MWIR is not possible to implement a bolometer, only a photodetector since the output signal that it would be obtained it would be insufficient. For LWIR, however, both a photodetector and a bolometer could be used.

In order to have actual values for the model, a comparison between the two bands considered, MWIR and LWIR, is performed selecting two detectors from SCD [62]. The detector for MWIR is a photodetector called Kinglet 640, while the detector for LWIR is a bolometer called Bird 384.

Property	**MWIR**	**LWIR**
Operative range [μm]	3.6-4.2	8-14
Weight [g]	300	27
Frame rate [FPS]	70	100
Quantum efficiency, η [%]	0.7	1
Pixel size, Ps [μm]	15	25
Binning factor	1	4
Array nxm	640x512	384x288
Fill factor, ff [%]	0.8	0.8
NETD$_{ground}$ [K]	0.023	0.044
f-number	1.464	1.708
focal length, f [m]	0.105	0.14
diameter, D [m]	0.072	0.082
GSD [m]	100	250
satellite integration time, t_i [ms]	14.3	35.8
thermal time constant, TTC [ms]	-	10
Detectivity, DET [W^{-1}]	1.582 $\times 10^{13}$	1.634 $\times 10^{11}$
NETD$_{space}$ [K] @ 270 to 310 K	0.327 to 0.075	0.071 to 0.046
Ground radiant flux [e$^-$] @ 270 to 310 K	(0.392 to 2.282)$\times 10^6$	(1.218 to 2.424) $\times 10^9$
SNR @ 270 to 310 K	63 to 368	781 to 1569

Table 8.1: Actual case MWIR vs LWIR.

Several values from Table 8.1 must be commented. As it was expected, the GSD in LWIR is more than two times the GSD for MWIR, therefore, the loss of spatial resolution to accomplish the dimensional and diffractive requirement is very important and must be taken into account. Because of the increase in GSD, the integration time in LWIR is almost three times the one for MWIR which allows to use a bolometer with a thermal time constant of 10 *ms*. Moreover, the NETD achieved in both bands is similar for high ground temperatures, but when this temperature decreases, the NETD in LWIR becomes much lower than in MWIR, although in any case, for both bands is good enough to perform the observation. In regards to the SNR, the signal is clearer in LWIR, this is due to the larger ground radiant flux in this band despite the lower detectivity of the bolometer. One should pay special attention to the MWIR for low ground temperatures as the SNR is lower than 100, which is, in general, the minimum value established to perform good results. Finally, it should be outlined the fact that the bolometer weights 11 times less, which means that the cost to put the satellite in orbit is 11 time less when compared to the photodetector.

So, many advantages can be obtained if OUFTI-Next becomes into a dual band imager. Firstly, measures could be taken for many different environmental conditions, MWIR cameras perform better for clear-weather and higher humidities while LWIR applications operate good under bad weather conditions such as fog, dust and haze. Furthermore, while MWIR cameras have a greater contrast, which allows to perceive better details, and a lower GSD, which implies higher spatial resolution, in LWIR a bigger sensitivity is procured, which allows to appreciate cooler bodies and making observations during the night. Combining all these benefits, the observation made would be of a higher quality and the availability of the system would be increased.

The dual band system could be implemented in the 3U CubeSat by using a dualband camera since the available room to install both optical systems separated is not enough. The MWIR and LWIR imager could be separated in case of increasing the dimensions of the satellite. For a 6U CubeSat (30cm x 20cm x 10cm) the cameras could be placed one next to the other. These options need of course to be studied in more detail and could be performed for next researchers.

A | Albedo

This appendix contains the plots that show the reflectivity of the different materials studied in order to estimate Earth's albedo, clustered in their respective groups:

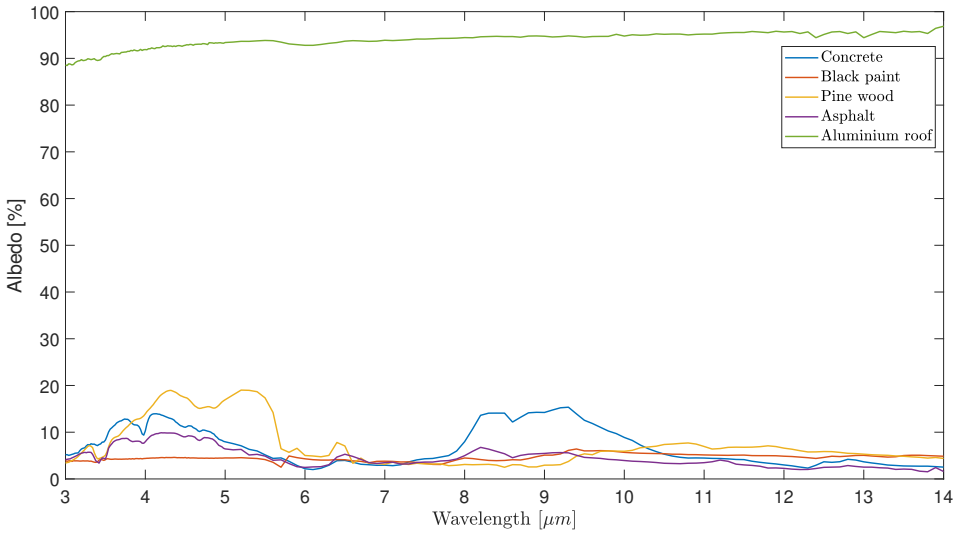

Figure A.1: Albedo vs wavelength in man made materials.

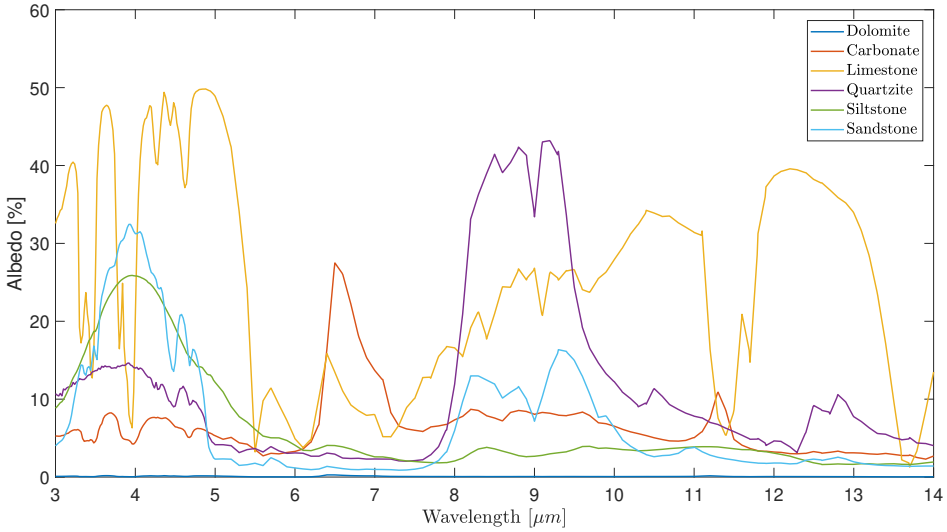

Figure A.2: Albedo vs wavelength in rocks.

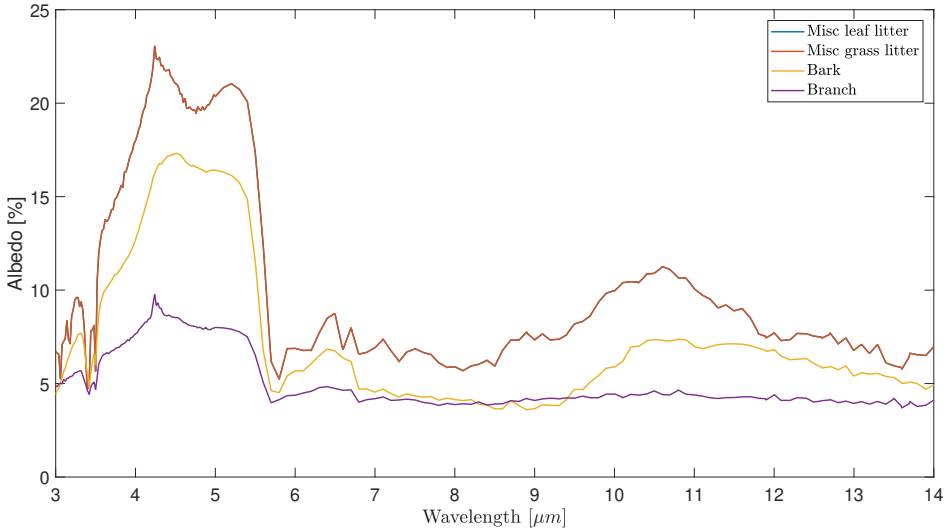

Figure A.3: Albedo vs wavelength in non-living plants.

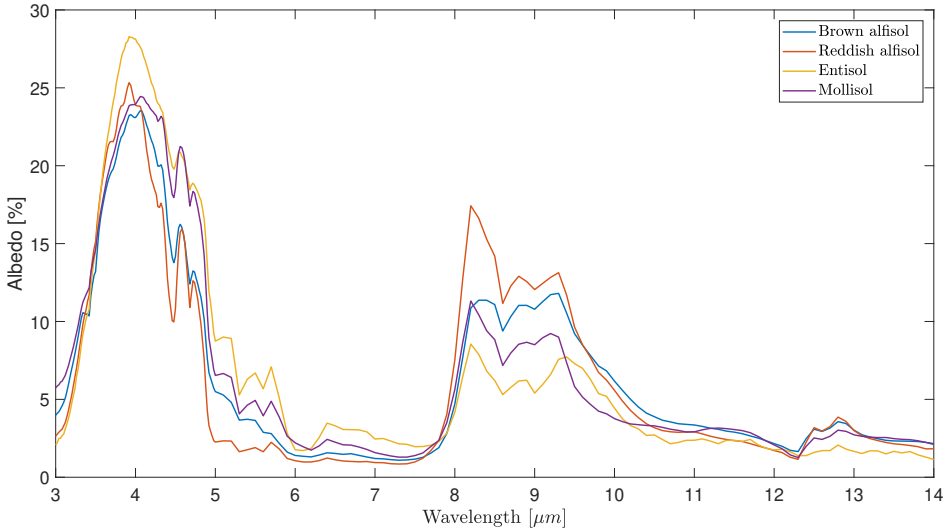

Figure A.4: Albedo vs wavelength in soils.

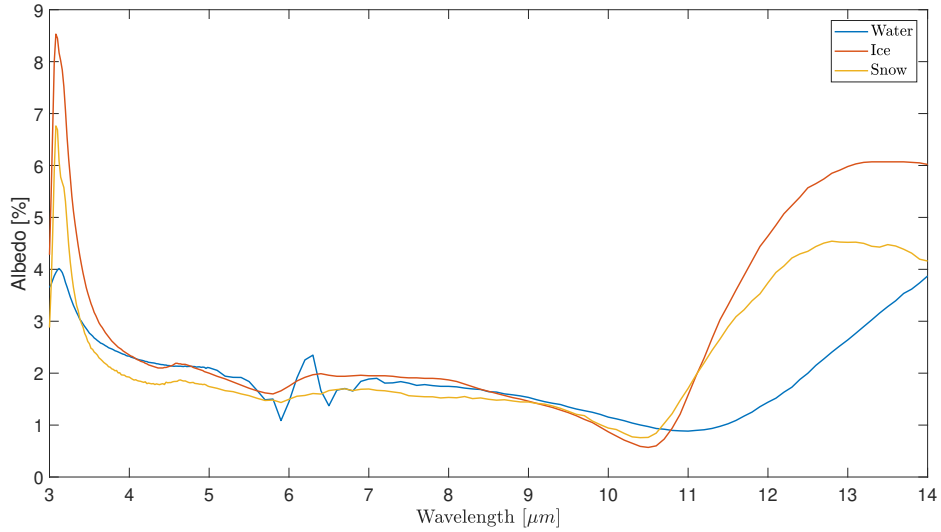

Figure A.5: Albedo vs wavelength in water.

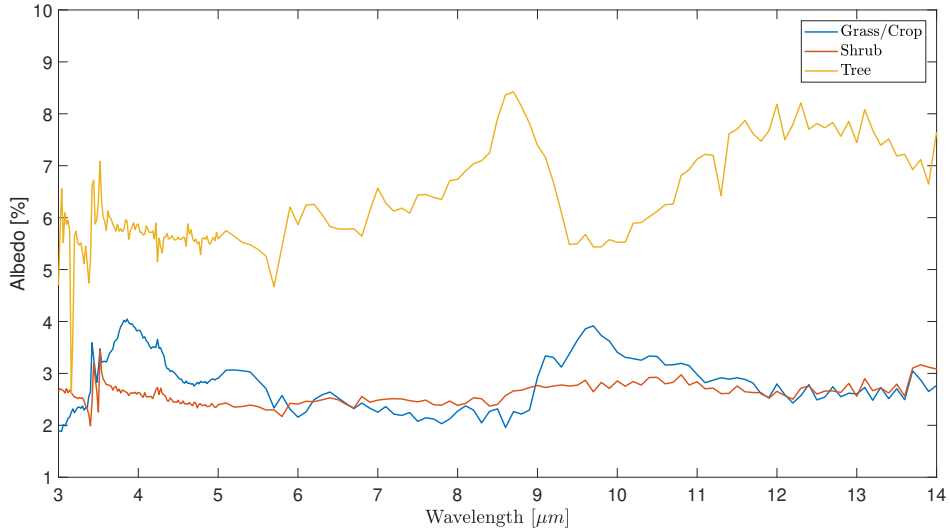

Figure A.6: Albedo vs wavelength in vegetation.

B | Ground emissivity

This appendix shows the emissivities of the rest of IGBP global cover lands. In order to find their definition see [6].

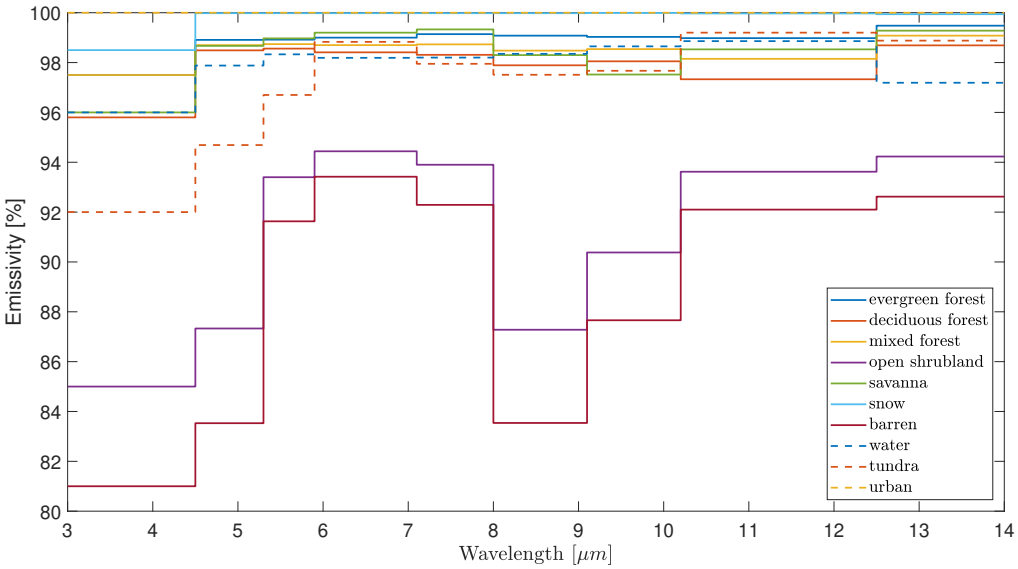

Figure B.1: Emissivity vs wavelength for studied cover lands [6].

C | Matlab codes

Spectral radiance of a black body

```
function Ls=spectral_radiance(wav,T)
%% Input parameters:
    % wav=waveband [m]
    % T=Temperature of the BB [K]
%% Calculation
% Constants
h = 6.62607004e-34;  %[J*s=m^2*kg/s] Planck's constant
c = 2.99792458e8;    %[m/s] Speed of light
k = 1.38064852e-23;  %[J/K=m^2*kg*s^(-2)*K^(-1)] Boltzmann's
   constant
% Obtaining spectral radiance
Ls = 2.*h*c*c./(wav.^5.*(exp(h.*c./(wav.*k.*T))-1.))*1e-6; %[
   W/(sr*m^2*micron)]
```

Radiometric budget

```
function [Ls_out_albedo, Ls_out_earth, Ls_payload]=
   Radiometric_budget(band, wav_initial, wav_end, Ts, Te1,
   Te2, Tpay1, Tpay2, soil, epsilon)
%% Input parameters:
    % band=Band of study
        %if MWIR -> band=1
        %if LWIR -> band=2
    % wav_initial=minimum wavelength of the studied band [m]
    % wav_end=maximum wavelength of the studied band [m]
    % Ts=Sun temperature [K]
    % Te1=Earth minimum temperature expected [K]
    % Te2=Earth maximum temperature expected [K]
    % Tpay1=Payload minimum temperature expected [K]
    % Tpay2=Payload maximum temperature expected [K]
    % soil=Type of soil considered
        %evergreen forest=1
        %deciduous forest=2
        %mixed forest=3
        %closed shrubland=4
        %open shrubland=5
        %savanna=6
```

```
20          %grassland=7
21          %permanent wetland=8
22          %cropland=9
23          %natural mosaic=10
24          %snow=11
25          %barren=12
26          %water=13
27          %tundra=14
28          %urban=15
29      %epsilon=emissivity of the lenses
30  %% Calculation
31  wav=wav_initial:0.005e-6:wav_end; %m
32  %% EXTERNAL FLUXES %%
33  % Obtain the atmospheric transmittance model
34  if band==1
35      TR=transmittance_MWIR_620 (wav);
36  elseif band==2
37      TR=transmittance_LWIR_1000(wav);
38  end
39  % FLUX DUE TO THE ALBEDO
40  % Sun parameters
41  r_sun=695510;  %[km]
42  d_sun_earth=149597870;  %[km]
43  % Obtaining solid angle Earth-Sun
44  sa_se=solid_angle(r_sun,d_sun_earth); %[sr]
45  % Obtaining the albedo
46  if band==1
47      albedo=albedo_MWIR(wav);
48  elseif band==2
49      albedo=albedo_LWIR(wav);
50  end
51  % Obtaining the spectral radiance emitted by the Sun
52  [Ls_sun]=spectral_radiance(wav,Ts); %[W/(sr*m^2*micron)]
53  % Spectral radiance that reaches the top of Earth's
       atmosphere
54  Ls_above_atm=Ls_sun*sa_se; %[W/(m^2*micron)]
55  % Spectral radiance reflected by the Earth throught the
       atmosphere supposing that surface receiving and reflecting
        albedo is half hemisphere
56  Ls_out_albedo=Ls_above_atm.*TR.*TR.*albedo./(2*pi); %[W/(sr*m
       ^2*micron)]
57  % FLUX DUE TO THE EARTH AS A BLACK BODY
58  % Obtain Ground emissivity for that soil
59  if band==1
60      [GE]=Ground_emissivity_MWIR(soil,wav);
61  elseif band==2
62      [GE]=Ground_emissivity_LWIR(soil,wav);
63  end
```

```
% Obtain the spectral radiance emitted by Earth
for Te=Te1:10:Te2
[Ls_earth]=spectral_radiance(wav,Te); %[W/(sr*m^2*micron)]
% Spectral radiance emitted by Earth throughout the
   atmosphere
Ls_out_earth=Ls_earth.*TR.*GE; %[W/(sr*m^2*micron)]
end
%% INTERNAL FLUXES %%
% FLUX DUE TO THE PAYLOAD OF THE SATELLITE
% Obtain the spectral radiance emitted by the payload
for Tp=Tpay1:10:Tpay2
[Ls_payload]=spectral_radiance(wav,Tp)*epsilon; %[W/(sr*m^2*
   micron)]
end
```

Optics

```
function [f,D,f_number,sa_optics,etendue,n]=Optics(band,
   wav_end,Px,GSD,H)
%% Input parameters:
    % band=Band of study
        %if MWIR -> band=1
        %if LWIR -> band=2
    % wav_end=maximum wavelength of the studied band [m]
    % Px=Pixel size [m]
    % GSD=Desired Ground Sampling Distance [m]
    % H=Height [km]
%% Calculation
H=H*1e3;
theta=atan(GSD/H); %[rad]
if band==1
    n=1;
elseif band==2
    n=2;
end
Ad=n*Px^2; %[m]
% Calculating the optics
syms f D f_number
eqn1 = f_number == n*Px/(2.44*wav_end); %Max number possible
   of f-number (<=)
eqn2 = f == n*Px/tan(theta); %[m]
eqn3 = D == f/f_number; %[m]
sol = solve([eqn1, eqn2, eqn3], [f, D, f_number]);
% Focal length
f=vpa(sol.f); %[m]
if f>0.15
    fprintf('WARNING: the focal length is exceeding the
       dimensional limits \n')
end
```

```
% Diameter
D=vpa(sol.D); %[m]
if D>0.1
    fprintf('WARNING: the diameter is exceeding the
       dimensional limits \n')
end
% f-number
f_number=vpa(sol.f_number);
if f_number<1.5
    fprintf('WARNING: the f-number might be lower than the
       achievable number \n')
end
% Solid angle
sa_optics=pi/4*1/f_number^2; %[sr]
% Etendue
etendue=vpa(Ad*sa_optics); %[sr*m^2]
```

Signal and SNR

```
function [Power_gr, F_ph_gr, ti, te, S_ground, detectivity,
   SNR]=SNR_function(band, wav_ini, wav_end, Ts, Te1, Te2,
   Tpay1, Tpay2, soil, epsilon, H, tau, q_eff, FR, Px, ff,
   GSD, NETD_gr, wav_ini_NETD, wav_end_NETD, Te_NETD, ff_NETD
   , zeta)
%% Input parameters:
    % band=Band of study
        %if MWIR -> band=1
        %if LWIR -> band=2
    % wav_ini=minimum wavelength of the studied band [m]
    % wav_end=maximum wavelength of the studied band [m]
    % Ts=Sun temperature [K]
    % Te1=Earth minimum temperature expected [K]
    % Te2=Earth maximum temperature expected [K]
    % Tpay1=Payload minimum temperature expected [K]
    % Tpay2=Payload maximum temperature expected [K]
    % soil=Type of soil considered
    % epsilon=emissivity of the lenses
    % H=height [km]
    % tau=transmittance of the optics
    % q_eff=quantum efficiency
    % FR=Frames rate of the detecotr [FPS]
    % Px=Pixel size [m]
    % ff=fill factor
    % GSD=Desired Ground Sampling Distance [m]
    % NETD_gr=manufacturer Noise Equivalent Temperature
       Difference [mK]
    % wav_ini_NETD=min. wavelength of the band used to
       measure NETD [m]
    % wav_end_NETD=max. wavelength of the band used to
```

```
        measure NETD [m]
    % Te_NETD=BB temperature for which NETD is calculated [K]
    % ff_NETD=Fill factor for which NETD is calculated [K]
    % zeta=optics filter coefficient
%% Calculations
wav_interval=wav_ini:0.1e-6:wav_end; %[m]
Te_interval=Te1:10:Te2;  %[K]
Tp_interval=Tpay1:10:Tpay2;  %[K]
% Constants
C=1.20173e6; %[A/(m^2*K^2)] Richardson constant
c=299792458; %[m/s] Speed of light
k = 1.38064852e-23;  %[J/K=m^2*kg*s^(-2)*K^(-1)] Boltzmann's
   constant
h = 6.62607004e-34;  %[J*s=kg*m^2/s] Planck's constant
mu=398600.4418; %[km^3/s^2] Gravitational parameter
Qe=1.6021766208e-19; %[C] Electron electric charge
R_earth=6378; %[km] Earth radius
w_earth=7.2921159e-5; %[rad/s] Angular velocity of the Earth
% Optics
[f,D,f_number,sa_optics,et,n]=Optics(band,wav_end,Px,GSD,H);
Ad=n*ff*Px^2;  %[m^2]  Detective area
%% INTEGRATION TIME %%
% Orbital period
a=H+R_earth; %[km]
T0=2*pi*sqrt(a^3/mu); %[s]
% Spacecraft velocity
Vsat=(2*pi/T0-w_earth)*a; %[km/s]
% Integration time
ti=GSD/(1000*Vsat); %[s]
%% SIGNAL %%
%% RADIANT FLUX FOR 1 PIXEL
% Albedo
if band==1
    Power_alb=Int_alb_W_MWIR(Ts,wav_ini,wav_end)*et*tau; %[W]
elseif band==2
    Power_alb=Int_alb_W_LWIR(Ts,wav_ini,wav_end)*et*tau; %[W]
end
% Ground
for index_Te=1:numel(Te_interval)
    Te=Te_interval(index_Te);
if band==1
    Power_gr(index_Te)=Int_gr_W_MWIR(Te,soil,wav_ini,wav_end)
       *et*tau; %[W]
elseif band==2
    Power_gr(index_Te)=Int_gr_W_LWIR(Te,soil,wav_ini,wav_end)
       *et*tau; %[W]
end
end
```

```
% Payload
for index_Tp=1:numel(Tp_interval)
    Tp=Tp_interval(index_Tp);
Power_pay(index_Tp)=Int_pay_W(Tp,epsilon,wav_ini,wav_end)*et*
   tau; %[W]
end
% Amount of total power that reaches 1 pixel
for index_Te=1:numel(Te_interval)
for index_Tp=1:numel(Tp_interval)
Total_power(index_Te,index_Tp)=Power_alb+Power_gr(index_Te)+
   Power_pay(index_Tp); %[W]
end
end
%% PHOTON FLUX
% Photons flux albedo
if band==1
    F_ph_alb=Inte_alb_ph_MWIR(Ts,wav_ini,wav_end)*et*tau; %[
       photon/s]
elseif band==2
    F_ph_alb=Int_alb_ph_LWIR(Ts,wav_ini,wav_end)*et*tau; %[
       photon/s]
end
% Photons flux ground
for index_Te=1:numel(Te_interval)
    Te=Te_interval(index_Te);
if band==1
    F_ph_gr(index_Te)=Inte_gr_ph_MWIR(Te,soil,wav_ini,wav_end
       )*et*tau; %[photon/s]
elseif band==2
    F_ph_gr(index_Te)=Int_gr_ph_LWIR(Te,soil,wav_ini,wav_end)
       *et*tau; %[photon/s]
end
end
% Photons flux payload
for index_Tp=1:numel(Tp_interval)
        Tp=Tp_interval(index_Tp);
F_ph_pay(index_Tp)=Int_pay_photon(Tp,epsilon,wav_ini,wav_end)
   *et*tau; %[photon/s]
end
%% NUMBER OF PHOTONS
FR=1/FR; %[s]
%Exposure time
te=FR/2; %[s]
% Number of photons albedo
S_ph_albedo=F_ph_alb*te; %[photon/pixel]
% Number of photons ground
S_ph_ground=F_ph_gr*te; %[photon/pixel]
% Number of photons albedo
```

```
S_ph_payload=F_ph_pay*te; %[photon/pixel]
% NUMBER OF ELECTRONS %
% Signal obtained albedo
S_albedo=S_ph_albedo*q_eff; %[e-/pixel]
% Signal obtained albedo
S_ground=S_ph_ground*q_eff; %[e-/pixel]
% Signal obtained albedo
S_payload=S_ph_payload*q_eff; %[e-/pixel]
%% OBTAINING THE NETD %%
% Ground
syms Ls T wav
Ls = 2*h*c^2/(wav^5*(exp(h*c/(wav*k*T))-1)); %[W/(sr*m^3)]
%Differentiate with respect to the temperature
dLs_dT=diff(Ls,T); %[W/(sr*m^3*K)]
%Integrate with respecto to the wavelength
dL_dT=int(dLs_dT,wav,wav_ini_NETD,wav_end_NETD); %[W/(sr*m^2*
   K)]
dL_dT=vpa(subs(dL_dT,T,Te_NETD));
f_number_gr = 1;
Ad_NETD=ff_NETD*Px; %[m^2]
detectivity = vpa((4*(f_number_gr^2))/(Ad_NETD*dL_dT*pi*zeta*
   NETD_gr)); %[1/W]
%% SNR %%
SNR=detectivity*Power_gr;
```

NETD in space

```
function [NETD_space]=NETD_function(band, wav_end, Te1, Te2,
   tau, H, Px, ff, GSD, NETD_gr, wav_ini_NETD, wav_end_NETD,
   Te_NETD, ff_NETD, zeta)
%% Input parameters:
    % band=Band of study
        %if MWIR -> band=1
        %if LWIR -> band=2
    % wav_end=maximum wavelength of the studied band [m]
    % Te1=Earth minimum temperature expected [K]
    % Te2=Earth maximum temperature expected [K]
    % tau=transmittance of the optics
    % H=height [km]
    % Px=Pixel size [m]
    % ff=fill factor
    % GSD=Desired Ground Sampling Distance [m]
    % NETD_gr=manufacturer Noise Equivalent Temperature
       Difference [mK]
    % wav_ini_NETD=min. wavelength of the band used to
       measure NETD [m]
    % wav_end_NETD=max. wavelength of the band used to
       measure NETD [m]
    % Te_NETD=BB temperature for which NETD is calculated [K]
```

```
18      % ff_NETD=Fill factor for which NETD is calculated [K]
19      % zeta=optics filter coefficient
20  %% Calculation
21  % Optics
22  [f,D,f_number,sa_optics,et,n]=Optics(band,wav_end,Px,GSD,H);
23  Ad=n*ff*Px^2;  %[m^2]  Detective area
24  %% NETD IN GROUND %%
25  syms Ls T wav
26  Ls = 2*h*c^2/(wav^5*(exp(h*c/(wav*k*T))-1)); %[W/(sr*m^3)]
27  %Differentiate with respect to the temperature
28  dLs_dT=diff(Ls,T); %[W/(sr*m^3*K)]
29  %Integrate with respecto to the wavelength
30  dL_dT=int(dLs_dT,wav,wav_ini_NETD,wav_end_NETD); %[W/(sr*m^2*
        K)]
31  dL_dT=vpa(subs(dL_dT,T,Te_NETD)); %[W/(sr*m^2*K)]
32  f_number_gr = 1;
33  Ad_NETD=ff_NETD*Px^2; %[m^2]
34  detectivity = vpa((4*(f_number_gr^2))/(Ad_NETD*dL_dT*pi*zeta*
        NETD_gr)); %[1/W]
35  %% NETD IN SPACE %%
36  Te_dL_dT = Te1:10:Te2;
37  if wav_end==4.2
38      dL_dT=differentiate_L_respect_T_36_42(Te_dL_dT); %[W/(sr*
            m^2*K)]
39  elseif wav_end==5
40      dL_dT=differentiate_L_respect_T_44_50(Te_dL_dT); %[W/(sr*
            m^2*K)]
41  elseif wav_end==12
42      dL_dT=differentiate_L_respect_T_80_120(Te_dL_dT); %[W/(sr
            *m^2*K)]
43  end
44  NETD_space=(4*f_number^2)./(Ad*dL_dT.*pi*zeta*detectivity*tau
        ); %[K]
```

Bibliography

[1] Nasa's 'space botanist' gathers first data. [Online]. Available: https://www.nasa.gov/feature/jpl/nasa-s-space-botanist-gathers-first-data

[2] "Cubesat design specification," *Rev. 13. CubeSat Cal Poly SLO*, 2018.

[3] A. Kellens, "Thermal design of the oufti-next mission."

[4] J. R. Howell, M. P. Menguc, and R. Siegel, *Thermal radiation heat transfer*. CRC press, 2015.

[5] "Ir transmission spectra," data based on observations obtained at the Gemini Observatory, which is operated by the Association of Universities for Research in Astronomy, Inc., under a cooperative agreement with the NSF on behalf of the Gemini partnership: the National Science Foundation (United States), National Research Council (Canada), CONICYT (Chile), Ministerio de Ciencia, Tecnología e Innovación Productiva (Argentina), Ministério da Ciência, Tecnologia e Inovação (Brazil), and Korea Astronomy and Space Science Institute (Republic of Korea). [Online]. Available: https://www.gemini.edu/sciops/telescopes-and-sites/observing-condition-constraints/ir-transmission-spectra

[6] A. Wilber, D. Kratz, and S. Gupta, "Surface emissivity maps for use in retrievals of longwave radiation satellite," *NASA Langley Research Center: Hampton, VA, USA*, 1999.

[7] E. M. Conwell, "Properties of silicon and germanium," *Proceedings of the IRE*, vol. 40, no. 11, pp. 1327–1337, 1952.

[8] Y. Bertrand, "Space validation of infrared materials for multispectral imager onboard a cubesat mission."

[9] Germanium. [Online]. Available: http://www.tydexoptics.com/pdf/Germanium.pdf

[10] High transmission silicon for infrared optical applications. [Online]. Available: http://www.topsil.com/media/123122/hitran_application_note_october2013.pdf

[11] Optical constant of schott - irg. [Online]. Available: https://refractiveindex.info/?shelf=glass&book=SCHOTT-IRG&page=IRG27

[12] U. D. of Health, H. Services, and U. D. of Agriculture, "2015-2020 dietary guidelines for americans." 2015.

[13] F. Food and A. O. of the United Nations, "Crops and drops: Making the best use of water for agriculture." 2002.

[14] J. Gliński, J. Horabik, and J. Lipiec, *Encyclopedia of agrophysics*. Springer Heidelberg, 2011.

[15] J. Pritchard, "Turgor pressure. els," 2001.

[16] S. Y. Lisar, R. Motafakkerazad, M. M. Hossain, and I. M. Rahman, "Water stress in plants: causes, effects and responses," in *Water stress*. Intechopen, 2012.

[17] New nasa mission to detect plant water use from space. [Online]. Available: https://www.nasa.gov/feature/jpl/new-nasa-mission-to-detect-plant-water-use-from-space

[18] E. Ghidoli, "Feasibility of earth cubesat observation in mwir window."

[19] D. Schklar, "Oufti-next nanosatellite: Feasibility study and mission assessment."

[20] D. Calozet, "Study of a ir reflective optical system for earth observation from a 3u cubesat."

[21] A. Riera Salva, "Oufti-next: Design of refractive lenses for an infrared camera."

[22] L. Suleimanova, "Compact thermal ir imager based on flat fresnel double lens for smart irrigation of agricultural fields-"oufti-next"."

[23] P. Remacle, "Study of a cooling system for a cubesat infrared detector."

[24] C. Dandumont, "From mission analysis to systems engineering of the oufti-next nanosatellite."

[25] Cubesatshop. 3-unit cubesat structure. [Online]. Available: https://www.cubesatshop.com/product/3-unit-cubesat-structure/

[26] "28.3Oct. 2010.

[27] A. Bejan, *Convection heat transfer*. John wiley & sons, 2013.

[28] H. S. Carslaw and J. C. Jaeger, *Conduction of heat in solids*. Oxford: Clarendon Press, 1959, 2nd ed., 1959.

[29] A. Le Van, "Integrated thermal design of oufti-next."

[30] J. M. Palmer and B. G. Grant, *The art of radiometry*. SPIE press Bellingham, 2010.

[31] R. C. Weast, M. J. Astle, W. H. Beyer *et al.*, *CRC handbook of chemistry and physics*. CRC press Boca Raton, FL, 1988, vol. 69.

[32] J. Byrnes, *Unexploded ordnance detection and mitigation*. Springer Science & Business Media, 2008.

[33] Evaluating the next generation - airborne thermal camera. [Online]. Available: http://cornerstonemapping.com/wp-content/uploads/2016/04/ASPRS_thermal_2012_web_ver.pdf

[34] Sun fact sheet. [Online]. Available: https://nssdc.gsfc.nasa.gov/planetary/factsheet/sunfact.html

[35] Earth fact sheet. [Online]. Available: https://nssdc.gsfc.nasa.gov/planetary/factsheet/earthfact.html

[36] M. Vollmer and K.-P. Möllmann, *Infrared thermal imaging: fundamentals, research and applications*. John Wiley & Sons, 2017.

[37] Steven D. Lord, "Nasa technical memorandum 103957."

[38] Air mass (solar energy). [Online]. Available: https://en.wikipedia.org/wiki/Air_mass_%28solar_energy%29

[39] Atmospheric water vapor. [Online]. Available: http://www.remss.com/measurements/atmospheric-water-vapor/

[40] C. Elachi and J. J. Van Zyl, *Introduction to the physics and techniques of remote sensing*. John Wiley & Sons, 2006, vol. 28.

[41] C. Barbier, *Remote Sensing. Chapter 7: Atmospheric remote sensing and radiative transfer*. University of Liege, 2019.

[42] U. G. P. O. N. SP811, *Guide for the Use of the International System of Units (SI)*, 1995.

[43] E. Secretariat, "Space environment," ECSS-E-10-04A, ESA Publications Division [Internet], 2000., Tech. Rep., 2008.

[44] A. M. Baldridge, S. Hook, C. Grove, and G. Rivera, "The aster spectral library version 2.0," *Remote Sensing of Environment*, vol. 113, no. 4, pp. 711–715, 2009.

[45] Types of soils and suitable crops. [Online]. Available: https://www.toppr.com/guides/science/soil/types-of-soil-and-suitable-crops/

[46] D. Grodent, *Earth atmosphere and space environment Syllabus*. University of Liege, 2018.

[47] S. Twomey, "Pollution and the planetary albedo," *Atmospheric Environment (1967)*, vol. 8, no. 12, pp. 1251–1256, 1974.

[48] J. R. Ballard, S. E. Howington, and S. C. Wilhelms, "Laboratory-based rainfall effects on lwir soil reflectance," *IEEE Geoscience and Remote Sensing Letters*, vol. 10, no. 3, pp. 627–630, 2012.

[49] M. Ramana, V. Ramanathan, D. Kim, G. Roberts, and C. Corrigan, "Albedo, atmospheric solar absorption and heating rate measurements with stacked uavs," *Quarterly Journal of the Royal Meteorological Society: A journal of the atmospheric sciences, applied meteorology and physical oceanography*, vol. 133, no. 629, pp. 1913–1931, 2007.

[50] Aster global emissivity database: 100 times more detailed than its predecessors. [Online]. Available: https://terra.nasa.gov/news/aster-global-emissivity-database-100-times-more-detailed-than-its-predecessors

[51] The climate data guide: Ceres: Igbp land classification. [Online]. Available: https://climatedataguide.ucar.edu/climate-data/ceres-igbp-land-classification

[52] V. Laborde, "Study and development of innovative optical systems for infrared remote sensing on board nano satellite."

[53] R. E. Fischer, B. Tadic-Galeb, P. R. Yoder, R. Galeb, B. C. Kress, S. C. McClain, T. Baur, R. Plympton, B. Wiederhold, and B. G. A. J, *Optical system design*. Citeseer, 2000, vol. 1, no. 2.

[54] Schott. [Online]. Available: https://www.us.schott.com/english/index.html

[55] M. J. Davis, W. James, G. Weber, and R. Jedamzik, "Irg 27: a" new" glass type for multi-band ir optics," in *Optical Components and Materials XIV*, vol. 10100. International Society for Optics and Photonics, 2017, p. 1010016.

[56] H. K. Raut, V. A. Ganesh, A. S. Nair, and S. Ramakrishna, "Anti-reflective coatings: A critical, in-depth review," *Energy & Environmental Science*, vol. 4, no. 10, pp. 3779–3804, 2011.

[57] J. Vilaboa Pérez, "Multi-band ir sensor for earth observation."

[58] G. B. Airy, "On the diffraction of an object-glass with circular aperture," *Transactions of the Cambridge Philosophical Society*, vol. 5, p. 283, 1835.

[59] A. Rogalski, *Infrared detectors*. CRC press, 2010.

[60] A. Daniels, *Field Guide to Infrared Systems, Detectors, and FPAs*. SPIE Press Bellingham, 2010.

[61] Z. Jakšić, *Micro and Nanophotonics for Semiconductor Infrared Detectors*. Springer, 2014.

[62] Semiconductor devices. [Online]. Available: http://www.scd.co.il/